Circuits and Systems
Mekelweg 4,
2628 CD Delft
The Netherlands
https://cas.tudelft.nl/

CAS-2022-5201446

M.Sc. Thesis

Cooperative Localization of Unmanned Aerial Vehicles using ADS-B

Xuzhou Yang B.Sc.

Abstract

As unmanned aerial systems (UAS) turn into a full-fledged industry, the sky will be much more crowded in the future. Large-scale UAV applications make reliable UAV navigation a pressing need. Traditionally, global navigation satellite system (GNSS) is extensively used as the primary positioning, navigation, and timing (PNT) service. However, GNSS is vulnerable to intentional radio interference such as spoofing, jamming, and repeating. Hence, alternative PNT (APNT) attracted many researchers' attention.

In this thesis, instead of GNSS signals, ADS-B signals from piloted aircraft are leveraged for UAV navigation. We propose a cooperative navigation strategy for multiple UAVs in GNSS-denied environments. It consists of: 1) a system-level, leader-follower cooperative strategy; 2) a sensor fusion algorithm for individual UAV navigation based on the extended Kalman filter. Furthermore, the effects of asynchronous clocks are studied and a joint relative positioning and synchronization algorithm is applied to tackle this problem.

Finally, Monte Carlo experiments in a multi-UAV scene are performed to verify the proposed algorithms. The results show that the proposed algorithms achieve a performance comparable to civilian GNSS on the selected data set and under the system assumptions we made. Moreover, the proposed cooperative navigation framework only needs one ground station of limited service capacity as external aid. Compared with large-scale, specialized terrestrial APNT service networks, our proposed framework is more flexible and the system can be deployed in areas without infrastructure.

Cooperative Localization of Unmanned Aerial Vehicles using ADS-B

Thesis

submitted in partial fulfillment of the
requirements for the degree of

Master of Science

in

Electrical Engineering

by

Xuzhou Yang B.Sc.
born in Jiangsu, China

This work was performed in:

Circuits and Systems Group
Department of Microelectronics
Faculty of Electrical Engineering, Mathematics and Computer Science
Delft University of Technology

Delft University of Technology

Delft University of Technology
Department of
Microelectronics

The undersigned hereby certify that they have read and recommend to the Faculty of Electrical Engineering, Mathematics and Computer Science for acceptance a thesis entitled **"Cooperative Localization of Unmanned Aerial Vehicles using ADS-B"** by **Xuzhou Yang B.Sc.** in partial fulfillment of the requirements for the degree of **Master of Science**.

Dated: 26 August 2022

Chairman: _____
dr. R.T. Rajan

Advisor: _____
dr. R.T. Rajan

Committee Members: _____
prof.dr.ir. A.J. van der Veen

_____
dr. J. Sun

Abstract

As unmanned aerial systems (UAS) turn into a full-fledged industry, the sky will be much more crowded in the future. Large-scale UAV applications make reliable UAV navigation a pressing need. Traditionally, global navigation satellite system (GNSS) is extensively used as the primary positioning, navigation, and timing (PNT) service. However, GNSS is vulnerable to intentional radio interference such as spoofing, jamming, and repeating. Hence, alternative PNT (APNT) attracted many researchers' attention.

In this thesis, instead of GNSS signals, ADS-B signals from piloted aircraft are leveraged for UAV navigation. We propose a cooperative navigation strategy for multiple UAVs in GNSS-denied environments. It consists of: 1) a system-level, leader-follower cooperative strategy; 2) a sensor fusion algorithm for individual UAV navigation based on the extended Kalman filter. Furthermore, the effects of asynchronous clocks are studied and a joint relative positioning and synchronization algorithm is applied to tackle this problem.

Finally, Monte Carlo experiments in a multi-UAV scene are performed to verify the proposed algorithms. The results show that the proposed algorithms achieve a performance comparable to civilian GNSS on the selected data set and under the system assumptions we made. Moreover, the proposed cooperative navigation framework only needs one ground station of limited service capacity as external aid. Compared with large-scale, specialized terrestrial APNT service networks, our proposed framework is more flexible and the system can be deployed in areas without infrastructure.

Acknowledgments

The process of completing the dissertation research is undoubtedly challenging and meaningful. Here, I would like to express my sincere appreciation to all the people who have helped me, for the patience and guidance they offered.

First of all, I would like to express my major thanks to my supervisor, dr. Raj Thilak Rajan, who patiently guided me and provided valuable suggestions along the way of my thesis project. I would like to thank dr. Junzi Sun, who showed me the exciting research field of ADS-B. In addition, I would also like to thank Zhonggang Li, Peiyuan Zhai and Rui Tang for the inspirations they gave me.

Finally, I would like to thank all my family and friends for their support during the two years of my graduate study.

Xuzhou Yang B.Sc.
Delft, The Netherlands
26 August 2022

Contents

List of Figures

List of Tables

List of Notations

The next list describes several symbols and operators that will be later used in this thesis.

a	Local scalar
A	Global constant scalar
$\boldsymbol{a}$	Column vector
$\boldsymbol{A}$	Matrix
$\mathcal{A}$	Set
$\mathbf{1}_N$	N-dimensional column vector of all ones
$\mathbf{0}_N$	N-dimensional column vector of all zeros
$\mathbf{0}_{M\times N}$	Matrix of all zeros with M rows and N columns
$\mathcal{R}^N$	Set of N-dimensional real column vectors
$\boldsymbol{I}_N$	Identity matrix with N rows and N columns
$\mathcal{R}^{M\times N}$	Set of $M \times N$ real matrices
$\|\cdot\|$	Euclidean norm operator
$(\cdot)^T$	Transpose operator
$(\cdot)^{-1}$	Inverse operator
$(\cdot)^*$	Conjugate operator
$\hat{(\cdot)}$	Estimate of some quantity
$\text{diag}(\cdot)$	Operator to make a diagonal matrix
$\otimes$	Quaternion multiplication operator
$\odot$	Element-wise matrix Hadamard product
$(\cdot)^{\odot N}$	Element-wise matrix exponent

1 Introduction

1.1 Background

As unmanned aerial systems (UAS) turn into a full-fledged industry, the sky will be much more crowded in the future. As predicted by Levitate Capital in [2], the highest unmanned aerial vehicles (UAV) market growth will be in logistics segment, from less than USD 0.1 billion (in the year 2020) to USD 33 billion (in the year 2030). Another report from ResearchAndMarkets.com investigated potential applications in other segments like agriculture, mining, media and entertainment, maintenance and inspections for important infrastructure, and defense [3].

Such large-scale application makes reliable UAV localization a pressing need. Traditionally, global navigation satellite system (GNSS) is extensively used as the primary positioning, navigation, and timing (PNT) service. However, GNSS is vulnerable to intentional or unintentional radio interference due to its low signal-to-noise ratio (SNR) [4]. Intentional interference has gained increasing attention because of the easy availability of software defined radios (SDR). There are three main types of intentional interference, namely jamming, spoofing, and repeating [1]. Jamming is to generate strong noise and overwhelm GNSS signals. A spoofing attack transmits counterfeit GNSS signals while a repeating attack broadcasts recorded GNSS-signals in large power after a fixed delay. These attacks target specifically the GNSS frequency bands and can cover from tens of meters to tens of kilometers, depending on the hardware, transmit power, and propagation environment.

Therefore, alternative PNT (APNT) service is of interest as it provides emergency service during GNSS outage. Many APNT solutions have been proposed, most of which are designed for piloted aircraft. They heavily rely on new or existing infrastructure operated by airports and air traffic control (ATC) centers. APNT for UAVs, however, utilize onboard sensors like camera, LiDAR extensively as well as short range RF technologies. A brief review on APNT techniques is presented in the next section.

1.2 State of the Art

1.2.1 APNT for Piloted Aircraft

One of the primary considerations in APNT systems is to maximize the use of legacy systems so that minimum impact is exerted on current investment and operations. As a result, APNT services proposed for piloted aircraft are often based on existing avionics and infrastructure.

Table 1.1: Comparison of three APNT techniques[1]

	Measurement	Capacity/Mode	Synchronization	Ground station number
DME	RTOF	Limited/active	Unnecessary	3
P-WAM	TDOA	Limited/active	Necessary	3
Pseudolite	Pseudorange	Unlimited/passive	Necessary	3

1.2.1.1 Distance Measurement Equipment (DME)

DME is a radio technology for slant distance measurement [5]. A airborne interrogator initiates an exchange by transmitting a pulsed signal; the ground transponder then replies after a fixed time delay. The reply is then received by the airborne interrogator and the exchange is completed. The time between signal transmission and reception at the airborne side is used to calculate the slant distance between the aircraft and the ground transponder. As positions of ground transponders are known, the aircraft can interrogate several ground transponders on different frequency bands to localize itself by triangulation. Researchers also proposed DME-based passive ranging (DMPR) which adds a ground interrogator to initiate a sequence of replies from DME ground transponders. Hence, any aircraft can use DME replies regardless of airborne exchange initiation.

The DME network is a mature system in operation, hence preferred by aviation stakeholders. Nominal DME relies on round-trip time measurements so there is no synchronization in the whole system. For DMPR, since the DME replies are always on, synchronization is needed to utilize time of transmission in DME frames. In [5], DMPR has demonstrated promising positioning accuracy to meet requirements of the Federal Aviation Administration (FAA) of the United States.

1.2.1.2 Passive Wide Area Multilateration (P-WAM)

P-WAM uses time difference of arrival (TDOA) configuration. This system has been applied in en-route navigation and approaching and now proposed by FAA as a potential APNT architecture. As a passive localization system, it consists of multiple ground stations that listen to signals from aircraft. Avionics transmit signals actively while at each P-WAM station receiving time is recorded. Recorded time stamps are then sent and evaluated at the fusion center to calculate aircraft positions by solving hyperbolic equations. The primary signal sources of P-WAM are aviation signals on 1090MHz band [6].

The accuracy of P-WAM depends on both TDOA precision and the dilution of precision (DoP). The former requires nanosecond level synchronization between ground stations. The latter is a metric of the geometric configuration of receivers. Thus, an optimal deployment strategy of P-WAM stations can be discussed. Further, the localization is done on the ground segment, so the results need to be sent to aircraft through a different communication service such as traffic information service broadcast (TIS-B).

1.2.1.3 Pseudolite Network

A pseduolite network is a set of ground stations that transmit GNSS-like signals. It is considered as an ground augmentation system for GNSS, which covers tens of kilometers [7]. However, it can be used independently for navigation as well [1]. Compared to authentic satellites, pseudolites provides signals with significantly higher SNR because they are much closer to aircraft. Their deployment and maintenance costs are lower than authentic satellites as well.

Like GNSS, a pseudolite network has unlimited service capacity. But its power level fluctuates with distance substantially, making it difficult for receivers to adjust to the signals. Moreover, it requires synchronization between ground-based stations on the nano-second level. As a consequence, an additional reference station and a specialized communication network are needed. In [8], researchers managed to obtain sub-nanosecond level synchronization. Pseudolites use time of arrival (TOA) method, just like authentic satellites. A receiver needs to solve its three-dimensional position and a clock offset so more than three pseudolites must be observed by receivers at the same time.

1.2.2 APNT for UAVs

With unmanned aerial vehicles being deployed in more and more applications, trusted operations of UAV have become increasingly important to all stakeholders in the industry. One essential element to ensure trusted operations is a robust navigation solution. Hence, like the situation in manned aviation, APNT for UAVs has also drawn researchers' attention, although the particular terms they prefer may be "navigation solutions in GNSS-denied area" or "navigation solutions during GNSS signal outage" instead of APNT.

Low operation and maintenance cost is often an advantage of unmanned aerial vehicles. However, this could also mean that UAVs are not likely to have expensive, high-performance avionics onboard like piloted aircraft. Most UAVs are just equipped with simple telemetry devices and low-cost, consumer grade sensors (e.g., inertial measurement units, GNSS receivers). Thus, UAV navigation systems are more vulnerable compared to that of manned aircraft. For example, most consumer grade GNSS receivers do not have the function of detecting and countering intentional radio interference, making UAVs more easily deceived by this kind of attack [9]. From another perspective, it is also not easy for UAVs to benefit from APNT services originally designed for manned aircraft, as these services, as mentioned above, all requires specific avionics. There are problems that prevent UAVs from using these avionics, such as size, weight, power consumption, regulation issues, and, of course, cost. Finally, with the number of UAVs in operation taking off, the capacity of existing APNT services may not be able to meet such demands [10].

Emerging APNT services for UAV broadly fall into two categories: APNT provided by external source and fully independent APNT with onboard sensors. In 2021, a company named *NextNav* proposed an terrestrial enhancement system called *TerraPoiNT* [11]. This system consists of terrestrial transmitters deployed in a service area and provide APNT service when GNSS is not available. This approach has shown promis-

ing results in a test held by the Department of Transportation of the United States, according to the company's website. Existing infrastructure can be used as APNT sources as well, such as cellular networks, Wi-Fi networks, and television or audio broadcast services. For example, cellular signal-based navigation has successfully obtained sub-meter level positioning accuracy [12]. Synchronization issues have also been looked at in [13]. Cellular base stations sometimes have coverage holes, which impairs the robustness of navigation. To counter this, UAV navigation/trajectory planning is proposed [14]. In [15], television and radio signals are treated from a signal of opportunity (SoOp) perspective, where researchers follow a two-step approach and extend the concept of simultaneous localization and mapping (SLAM) to radio-based navigation. In [15], UAVs first collaboratively surveyed SoOp signal sources in proximity with the aid of inertial sensors, GNSS, and inter-UAV communication devices. After some time GNSS becomes unavailable, these vehicles then utilize collaborative inertial radio SLAM (CIRSLAM) to continue navigation. The second step can be considered as providing some kind of APNT service. Furthermore, researchers developed and compared two different information fusion strategies for inter-UAV collaboration.

Fully independent navigation with onboard sensors of UAVs is a vast field of research, where navigation meets computer vision, optimization, and artificial intelligence. For example, in [16], researchers proposed a robust monocular visual-inertial odometry for UAV six degrees-of-freedom (DOF) state estimation. This work shows good long-term stability and robustness. Though this method only provides state estimates in some local navigation coordinate system (e.g., a coordinate system using takeoff position as origin and defining three axes based on some criterion), it is still useful in the sense of APNT. Autonomous vehicles can switch to this navigation solution when GNSS is unavailable, using the last reliable absolute position as the start point. Combining odometry information also enables more robust autonomous vehicles navigation in GNSS-degraded environment, where GNSS does not completely fail but experiences intermittent signal loss [17].

1.3 Goals

In this thesis, we explore the possibility of an APNT solution for UAVs with minimum infrastructure requirement. We do this by exploiting Automatic Dependent Surveillance–Broadcast (ADS-B) signals that are free-to-use from other piloted aircraft. However, there's no free lunch. Lacking important navigational information, ADS-B signals are not designed for navigation purposes and must be treated as signal of opportunity (SoOp). Moreover, piloted aircraft are not aware of the presence of UAVs, let alone cooperation or communication. To overcome these problems, an SoOp-based time difference of arrival (TDOA) configuration is applied. We further look at the potential of cooperation between UAVs that request for APNT service and propose a cooperative localization strategy based on inter-UAV communication networks.

The main goals of the thesis are:

- Analyze the feasibility of ADS-B SoOp and establish the corresponding data model;

- Propose a cooperative localization strategy for a network of UAVs;
- Propose an onboard sensor fusion algorithm for individual UAV navigation using low-cost sensors;
- Extend the cooperative localization strategy to a network of asynchronous UAVs and verify its robustness.

1.4 Outline

This thesis is structured as follows and shown in Fig.1.1:

- In Chapter 2, some preliminary knowledge is presented on ADS-B systems, GNSS localization, the extended Kalman filter, quaternion basics, and notation conventions used in this thesis.
- In Chapter 3, we exploit ADS-B signals as signal of opportunity (SoOp) and introduce an SoOp-based time difference of arrival (TDOA) configuration for receiver localization; a Newton-Raphson method is applied to solve the SoOp-based TDOA measurement equations.
- In Chapter 4, we propose a leader-follower strategy for cooperative localization of multiple UAVs based on inter-UAV networks. A sensor fusion algorithm based on the extended Kalman filter is proposed for individual UAV localization without GNSS service.
- In Chapter 5, we extend the leader-follower cooperative strategy to the circumstance where all UAVs and the ground station are asynchronous. The effects of local asynchronous clocks are discussed, by which the errors caused are identified. The joint relative positioning and synchronization algorithm is applied in order to make the cooperative localization framework robust against clock asynchrony.
- Chapter 6 concludes the thesis. The main contributions of this thesis are summarized and future research directions are discussed.

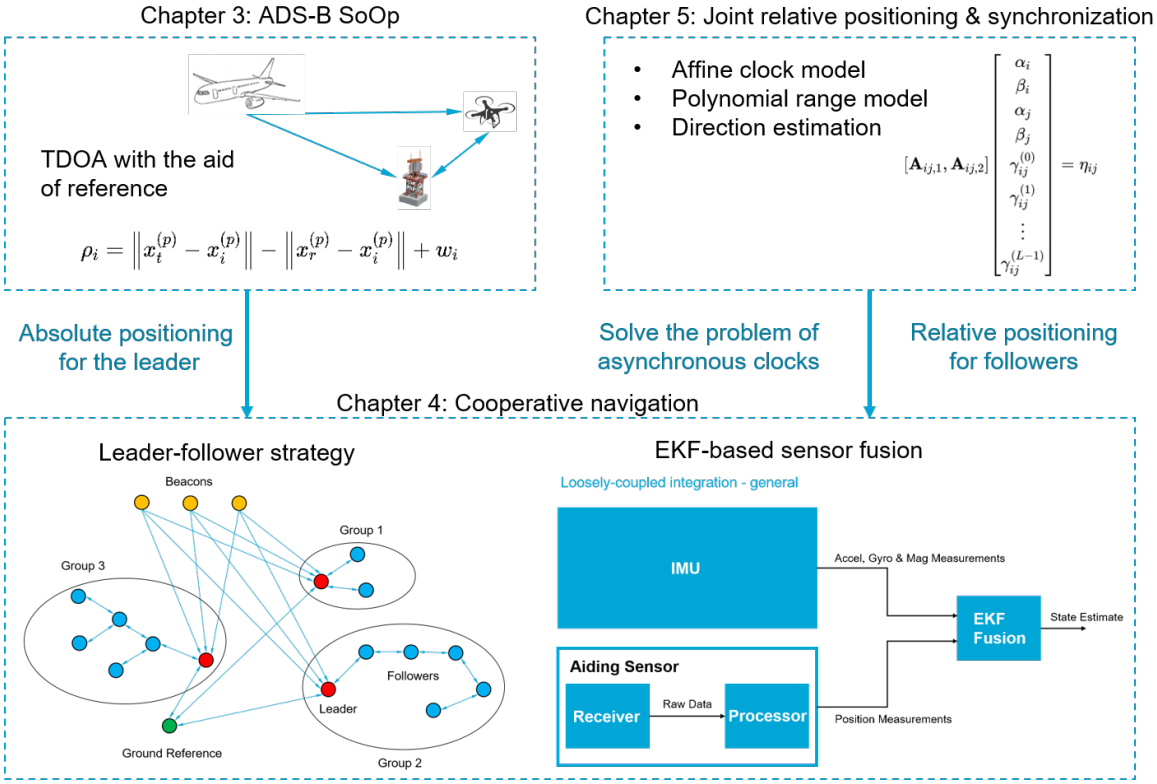

Figure 1.1: A brief schematic figure for thesis outline

2 Preliminaries

In this chapter, we present some preliminary knowledge. In Section2.1, we introduce the Automatic Dependent Surveillance–Broadcast (ADS–B) system and briefly touch ADS-B message decoding. In Section2.2, the localization method used in GNSS as well as its assumptions/requirements are presented. This helps the reader to get familiar with localization problems. In Section2.3, the definition and some fundamental properties of quaternions are presented. Quaternions are extensively used in orientation representation of rigid bodies. In Chapter4, the orientation of the UAV is parameterized by (unit) quaternions. In Section2.4, a review of the extended Kalman filter is presented, which is used in Chapter4.

2.1 Automatic Dependent Surveillance–Broadcast (ADS–B)

Automatic Dependent Surveillance - Broadcast is an surveillance technology that is used extensively in ATC applications. Aircraft broadcast ADS-B messages periodically with on-board Mode-S transponders, which include navigational information such as surface/airborne position, airborne velocity, call sign, operational status, etc. ADS-B enables ATC ground stations to track aircraft continuously in regions that are not covered by traditional radars, as its coverage can be greatly extended by ground-based or space-based ADS-B receivers. It is considered to be a key component of the future air transportation system and is mandated both by EUROCONTROL [18] in Europea and FAA [19] in the U.S. since 2020.

Prior to the introduction of ADS-B, ATC applications heavily relied on the primary surveillance radar (PSR) and the secondary surveillance radar (SSR). PSR provides slant distance as well as aircraft's azimuth information with respect to the radar location, while SSR provides aircraft's altitude and identity. However, inherent limitations of PSR and SSR technology hinder further improvement in accuracy and coverage. ADS-B is thus introduced to enhance situational awareness for both ATC controllers and pilots.

Now we briefly discuss about how to decode ADS-B messages. Most of the contents are summarized from [20].

2.1.1 Aircraft Identity Decoding

In navigation, we always need to differentiate signals coming from different sources. In every legal ADS-B message, the International Civil Aviation Organization (ICAO) address of an aircraft is encoded. This ICAO address is a unique registration number for every piloted aircraft in the world. So it is very handy to discriminate different aircraft by looking at the ICAO address.

2.1.2 Time of Arrival Decoding

ADS-B is not designed to contain any time of transmit information, which means we cannot directly calculate the signal propagation delay by finding the difference between time of transmit and time of arrival. As a highly standardized communication protocol, it is not feasible to arbitrarily change the message structure and add time of transmit information. Further, since aircraft broadcasting ADS-B signals are not aware of our UAVs, it is also not practical to send messages from UAVs to manned aircraft or to synchronize with manned aircraft.

2.1.3 Airborne Position Decoding

A typical airborne position message contains longitude, latitude, and altitude of an aircraft. It is trivial to decode altitude but longitude and latitude are encoded in Compact Position Reporting (CPR) format. One can use globally unambiguous position decoding or locally unambiguous position decoding. Globally unambiguous position decoding, without any prior information, always needs a pair of "odd" and "even" messages to calculate a globally correct position [20]. Locally unambiguous position decoding, on the other hand, requires a known reference position. The reference should be close to the decoded position, e.g., within a range of 180 nautical miles (NM). The advantage is that from every message one can decode a position.

2.1.4 Airborne Velocity Decoding

The airborne velocity message reports velocity decomposed in East-West, North-South and vertical directions. In the field of civil aviation, it is also common to compute a track angle without considering altitude changes. It is trivial to decode the message itself. But it is worth noting that only ground speed can be used in our application. The ground speed of aircraft is measured with respect to the ground, which is the sum of the true airspeed vector and the wind velocity vector.

2.2 GNSS Navigation

Global navigation satellite system (GNSS) refers to any satellite constellation that provides positioning, navigation, and timing (PNT) service. Existing constellations include GPS, Galileo, BeiDou, GLONASS, etc. GNSS is based on time of arrival (TOA) localization, a simplified setting of which is shown in Fig.2.1. A comprehensive introduction of GNSS navigation can be found in [21].

In Fig.2.1, the receiver at the surface of the earth can capture specially designed GNSS navigation signals from multiple satellites in view. GNSS signals contain many useful contents, including ranging signals and navigation messages. A ranging signal is a segment of code modulation signal tailored for high-precision time of arrival measurement. Ranging signals can also be used to identify which satellite is broadcasting since they are unique for each satellite. Two essential elements of navigation messages are time of transmission and ephemeris data. The time of transmission records when the ranging signal is initiated precisely by the satellite. The ephemeris data let the receiver

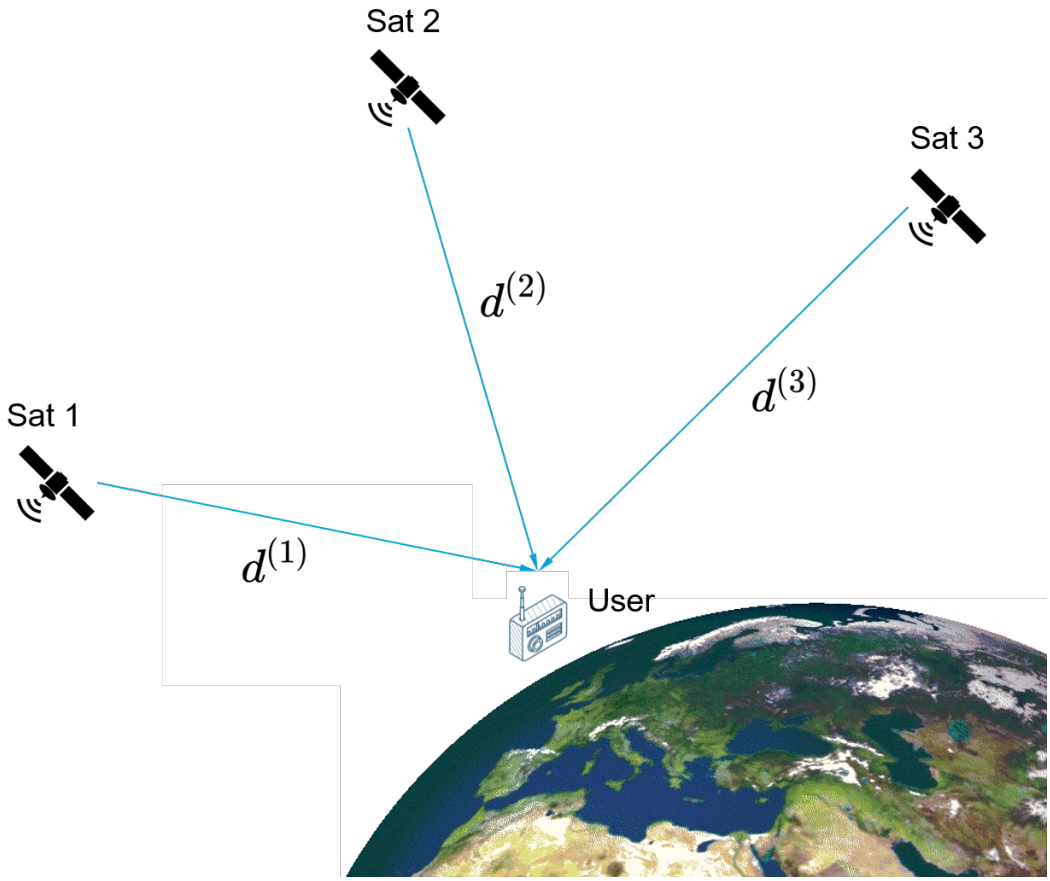

Figure 2.1: A simplified illustration of how GNSS works

be able to figure out the actual location of the satellite, which moves with about 3000 meters per second on orbit. Other information to enable precise measurement and error compensation are also included, but we only consider an simplified data model.

Here is the data model. Suppose the whole satellite constellation conforms to some standard time frame, and the time of transmission at the satellite side t_{tmt} and time of arrival at the receiver side t_{rcv} are both recorded under this frame. The travel distance of radio waves d from satellite to receiver can be calculated, assuming the propagation speed is the speed of light c. The relation of these quantities is given by

$$t_{rcv} - t_{tmt} = \frac{d}{c} = \frac{\|\boldsymbol{x}_{sat} - \boldsymbol{x}_u\|}{c} \tag{2.1}$$

However, the receiver is not necessarily synchronized to the GNSS standard time frame. Let us define the time of arrival measured with respect to the *local clock* of receiver t_u as the "true" t_{rcv} plus some clock bias b_u, given by

$$t_u = t_{rcv} + b_u \tag{2.2}$$

If the observation period is sufficiently small, the clock bias is modeled as constant across measurements from different satellites. Combining these two equations and

adding a residual error term ϵ_u, the complete pseudorange data model is given by

$$\tau_u = (t_u - t_{tmt})c = \|\boldsymbol{x}_{sat} - \boldsymbol{x}_u\| + b_u + \epsilon_u \tag{2.3}$$

where the newly introduced term ϵ_u incorporate errors caused by ionospheric propagation delay, tropospheric propagation delay, measurement noise, and other effects [22].

Our goal is to solve for $\boldsymbol{x}_u$ and b_u. Here t_{rcv} is measured using ranging signals. The satellite location $\boldsymbol{x}_{sat}$ and t_{tmt} are obtained from navigation messages. Unique ranging codes also help the receiver differentiate between satellites. Since the unknown user location is three-dimensional, there are four unknowns in total in the pseudorange equation. By accumulating pseudorange measurements with respect to different satellites, a system of equations in $\boldsymbol{x}_u$ and b_u can be obtained. To make it an overdetermined system, at least four satellites are required. In practice, Seven to eight satellites in view are preferred.

In this section, the working principle of GNSS is reviewed based on a simplified yet fundamental model. To summarize, from the receiver side the followings are needed:

- time of arrival (measured at the receiver);
- time of transmission (external information);
- satellite location (external information);
- information to differentiate between satellites;
- synchronization between the satellite and the receiver.

2.3 Quaternion Representation

The quaternion is an extension of the complex number. It is a commonly used parametrization of orientation. A quaternion is defined as

$$\boldsymbol{q} = q_0 + q_1 \cdot \boldsymbol{i} + q_2 \cdot \boldsymbol{j} + q_3 \cdot \boldsymbol{k} \tag{2.4}$$

where q_0 is the coefficient of the real part and q_1, q_2, q_3 are the coefficients of three imaginary parts. We usually omit the imaginary units $\boldsymbol{i}$, $\boldsymbol{j}$, $\boldsymbol{k}$ and write a quaternion in a compact form

$$q = \begin{bmatrix} q_0 \\ q_1 \\ q_2 \\ q_3 \end{bmatrix} \tag{2.5}$$

The multiplication of two quaternions $p = [p_0, p_1, p_2, p_3]^T$ and $q = [q_0, q_1, q_2, q_3]^T$ is defined as

$$p \otimes q = \begin{bmatrix} p_0 & -p_1 & -p_2 & -p_3 \\ p_1 & p_0 & -p_3 & p_2 \\ p_2 & p_3 & p_0 & -p_1 \\ p_3 & -p_2 & p_1 & p_0 \end{bmatrix} \begin{bmatrix} q_0 \\ q_1 \\ q_2 \\ q_3 \end{bmatrix} = \begin{bmatrix} q_0 & -q_1 & -q_2 & -q_3 \\ q_1 & q_0 & q_3 & -q_2 \\ q_2 & -q_3 & q_0 & q_1 \\ q_3 & q_2 & -q_1 & q_0 \end{bmatrix} \begin{bmatrix} p_0 \\ p_1 \\ p_2 \\ p_3 \end{bmatrix} \tag{2.6}$$

The conjugate of q is defined as

$$q^* = \begin{bmatrix} q_0 \\ -q_1 \\ -q_2 \\ -q_3 \end{bmatrix} \tag{2.7}$$

.

Given a vector $\boldsymbol{a}_{f1} \in \mathcal{R}^4$ expressed in the coordinate frame $f1$, and a quaternion q_{f1}^{f2} that describes the rotation from $f1$ to another coordinate frame $f2$, the same vector expressed in $f2$, denoted by $\boldsymbol{a}_{f2}$ is given by

$$\boldsymbol{a}_{f2} = q_{f1}^{f2} \otimes \boldsymbol{a}_{f1} \otimes (q_{f1}^{f2})^* \tag{2.8}$$

where $(q_{f1}^{f2})^*$ is the conjugate of q_{f1}^{f2}. This multiplication of the first two terms can be computed using 2.6, whose result is then right-multiplied by $(q_{f1}^{f2})^*$ and can be computed using 2.6 again.

If $\boldsymbol{a}_{f1} \in \mathcal{R}^3$, it is required to first augment $\boldsymbol{a}_{f1} = [a_1, a_2, a_3]^T$ to a four-dimensional vector by filling the first component with 0, given by

$$\boldsymbol{a}_{f1,aug} = \begin{bmatrix} 0 \\ a_1 \\ a_2 \\ a_3 \end{bmatrix} \tag{2.9}$$

.

2.4 Extended Kalman Filter

The Kalman filter-based sensor fusion approaches are extensively used. The Kalman filter is proposed under the assumption that the system model and the measurement model are both linear with white Gaussian noise. However, if the system model or the measurement relationship is inherently nonlinear, the Kalman filter needs to linearize about the current mean and covariance, which is called an extended Kalman filter [23].

Concretely, suppose we have a system or process governed by a nonlinear stochastic difference equation

$$\boldsymbol{x}_k = f(\boldsymbol{x}_{k-1}) + \boldsymbol{w}_{k-1} \tag{2.10}$$

where $\boldsymbol{x}_k \in \mathcal{R}^n$, $\boldsymbol{x}_{k-1} \in \mathcal{R}^n$ are state vectors at time instance k and $k-1$ respectively and random variable $\boldsymbol{w}_{k-1} \in \mathcal{R}^n$ is the process noise at time instance $k-1$. The measurement relationship relates the measurement vector $\boldsymbol{z} \in \mathcal{R}^m$ to the state, which is given by

$$\boldsymbol{z}_k = g(\boldsymbol{x}_k) + \boldsymbol{v}_k \tag{2.11}$$

where random variable $\boldsymbol{v}_k$ is the measurement noise at time instance k. The measurement relationship is also a nonlinear stochastic difference equation.

Please note that we model the process and measurement noise as additive. It is often assumed that they are both white noise and normally distributed with zero mean.

$$p(\boldsymbol{w}) \sim \mathcal{N}(0, \boldsymbol{Q}) \tag{2.12}$$
$$p(\boldsymbol{v}) \sim \mathcal{N}(0, \boldsymbol{R}) \tag{2.13}$$

The computation of the extended Kalman filter is very similar to the original Kalman filter in the linear-Gaussian case, only some quantities need to be alternated for the nonlinear models. A more detailed derivation can be found in [23]. First, we need to set the initial value for EKF, namely, $\hat{\boldsymbol{x}}_0$ and $\boldsymbol{P}_0$. We project the state estimate $\hat{\boldsymbol{x}}_{k-1}$ at time instant $k-1$ ahead to k by

$$\tilde{\boldsymbol{x}}_k = f(\hat{\boldsymbol{x}}_{k-1}) \tag{2.14}$$

without taking process noise $\boldsymbol{w}_k$ into consideration. The error covariance $\boldsymbol{P}_{k-1}$ is also projected ahead along with the state by

$$\tilde{\boldsymbol{P}}_k = \boldsymbol{F}_k \boldsymbol{P}_{k-1} \boldsymbol{F}_k^T + \boldsymbol{W}_k \boldsymbol{Q}_{k-1} \boldsymbol{W}_k^T \tag{2.15}$$

which, along with 2.14, are called the "prediction step" or time update of EKF. Here, $\boldsymbol{F}_k$ is the Jacobian matrix of the system model in 2.10 taken with respect to the state $\hat{\boldsymbol{x}}_{k-1}$ at time instant k, which indicates linearization about the state estimate from the last time instant. Similarly, $\boldsymbol{W}_k$ is the Jacobian matrix of the system model with respect to the noise random variable $\boldsymbol{w}_k$. It is an identity matrix because the noise is additive.

Then comes the "correction step" or measurement update. To fuse measurements the Kalman gain needs to be computed as following

$$\boldsymbol{K}_k = \tilde{\boldsymbol{P}}_k \boldsymbol{H}_k^T (\boldsymbol{H}_k \tilde{\boldsymbol{P}}_k \boldsymbol{H}_k^T + \boldsymbol{V}_k \boldsymbol{R}_k \boldsymbol{V}_k^T)^{-1} \tag{2.16}$$

where $\boldsymbol{H}_k$ is the Jacobian matrix of the measurement model in 2.11 with respect to the state $\tilde{\boldsymbol{x}}_k$ and $\boldsymbol{V}_k$, an identity matrix, is the Jacobian matrix of the measurement model with respect to the noise random variable $\boldsymbol{v}_k$. The estimate is updated with measurements as

$$\hat{\boldsymbol{x}}_k = \tilde{\boldsymbol{x}}_k + \boldsymbol{K}_k (\boldsymbol{z}_k - g(\tilde{\boldsymbol{x}}_k)) \tag{2.17}$$

The error covariance of the posterior estimate $\boldsymbol{x}_k$ at time instant k is also updated as

$$\boldsymbol{P}_k = (\boldsymbol{I} - \boldsymbol{K}_k \boldsymbol{H}_k) \tilde{\boldsymbol{P}}_k \tag{2.18}$$

Algorithm 1 The extended Kalman filter

Input: $\boldsymbol{x}_0$, $\boldsymbol{P}_0$, the sequence of data $\boldsymbol{z}_k$ ($k \in \{1, 2, 3, .., K\}$).
Output: State estimates $\boldsymbol{x}_k$, posterior covariance $\boldsymbol{P}_k$ and Kalman gains $\boldsymbol{K}_k$ ($k \in \{1, 2, 3, .., K\}$).

Begin
    Initialize $\boldsymbol{x}_0$ and $\boldsymbol{P}_0$ with initial states (position, velocity, etc.) of each target.
    For $k = 1$ to K **do**
        Project $\boldsymbol{x}_{k-1}$ to $\tilde{\boldsymbol{x}}_k$
        Project $\boldsymbol{P}_{k-1}$ to $\tilde{\boldsymbol{P}}_k$
        Compute $\boldsymbol{K}_k$
        Update $\tilde{\boldsymbol{x}}_k$ to $\boldsymbol{x}_k$ with $\boldsymbol{K}_k$ and $\boldsymbol{z}_k$
        Update $\tilde{\boldsymbol{P}}_k$ to $\boldsymbol{P}_k$ with $\boldsymbol{K}_k$
    end
end

Signal of Opportunity Navigation using ADS-B

3

In this chapter, we consider how to use ADS-B signals as signal of opportunity (SoOp) for navigation. First, we analyze what information can be extracted from received ADS-B signals and compare with the available information in GNSS navigation problem. Our analysis shows that ADS-B SoOp lacks certain important information, hence the localization configuration in GNSS does not work in the case of ADS-B SoOp. In order to solve this problem, an SoOp-based time difference of arrival (TDOA) configuration from [24] is applied. Finally, we show that the SoOp-based TDOA localization is in essence solving a system of nonlinear equations. Via reformulation, this problem can be solved using the Newton-Raphson method [22].

3.1 Analysis of ADS-B SoOp

ADS-B signals have been used in UAV localization, being a promising technology for future UAV surveillance and traffic management. In most works, such as [25] and [26], it is proposed that passive localization of the UAV is performed with ground infrastructure, whose results are then routed back to the UAV. To the best of the author's knowledge, however, few works exploit ADS-B signal of opportunity and use it in a similar way to GNSS.

Signal of opportunity (SoOp) navigation refers to the use of any signal for navigation, which is normally intended for purposes other than navigation. SoOp navigation can leverage signals such as FM/AM radio signals, TV signals, and cellular signals in order to improve navigation availability.

ADS-B signals are also among potential signal of opportunity. ADS-B SoOp has several advantages: 1) it is abundant in areas with high density air traffic; 2) ADS-B signals can be received from a distance of up to tens of kilometers [27]; 3) it usually has a higher signal-to-noise ratio (SNR) than that of GNSS signals [28]; 4) it does not need survey of signal sources in advance since locations of ADS-B sources can be obtained from received signals. In this thesis, we explore the possibility of ADS-B SoOp as an external aiding source for UAV navigation.

Recall from Section2.1, the following information can be obtained from received ADS-B signals:

- airborne position of the signal source (piloted aircraft);
- airborne velocity of the signal source (piloted aircraft);
- ICAO registration number that can be used to distinguish different sources;
- time of arrival measured at the receiver side.

Compare the available navigation information of ADS-B SoOp with that of GNSS, as mentioned in Section2.2, we find that time of transmission information is missing for ADS-B SoOp. Actually, according to the ADS-B implementation standard, time of transmission information is not contained in the broadcast messages. Hence, the requirement of time of transmission information must be lifted in ADS-B SoOp. Furthermore, aircraft transmitting ADS-B signals are not aware of potential SoOp users. Hence, it is not practical to establish communication between aircraft with ADS-B and SoOp users or synchronize them in any way. Third, ADS-B SoOp users should only be equipped with receivers and not transmit any signal on the protected frequency band where ADS-B service sits. Given the problems about ADS-B SoOp, it can be seen that the traditional TOA localization method used in GNSS will not work because it requires the availability of time of transmission information at the user side as well as synchronization between the user and signal providers. Therefore, in this chapter, a different configuration, namely the SoOp-based TDOA is used [24].

3.1.1 List of Assumptions

In this thesis, UAVs requesting for APNT service and explioting SoOp in proximity are referred to as *targets*. Piloted aircraft that provide ADS-B signals are referred to as *beacons*. A *reference* station is also deployed to aid UAV navigation. For example, in Fig.3.1 the aircraft broadcasting ADS-B signals is a *beacon*; the ground station is considered a *reference*; The UAV on the right with bidirectional link to ground station is, apparently, a *target*.

1. Targets, beacons, and the reference are all synchronized.
2. Targets can distinguish signals from different beacons.
3. Targets can communication with the reference on a channel other than that of ADS-B.
4. During an observation period, the network consisting of targets, beacons, and the reference is assumed to be static.
5. The system works under line-of-sight conditions without considering multi-path propagation or shading.

3.2 SoOp-based TDOA

For a mobile target, a set of beacons can be used for navigation with the aid of the reference station, whose location is very well known. Let us define the state of the target as $\boldsymbol{x}_t \in \mathcal{R}^6$, state of i-th beacon $\boldsymbol{x}_i \in \mathcal{R}^6$ $(i \in \{1, 2, ..., N\})$, and state of the reference $\boldsymbol{x}_r \in \mathcal{R}^6$. Further, define $\boldsymbol{x}^{(p)} \in \mathcal{R}^3$ and $\boldsymbol{x}^{(v)} \in \mathcal{R}^3$ as the position and velocity vector for a target, a beacon, or a reference, respectively.

The geometric interpretation of SoOp-based TDOA is shown in Fig.3.1. For simplicity, we assume all targets, beacons, and references involved are *synchronized*, which is

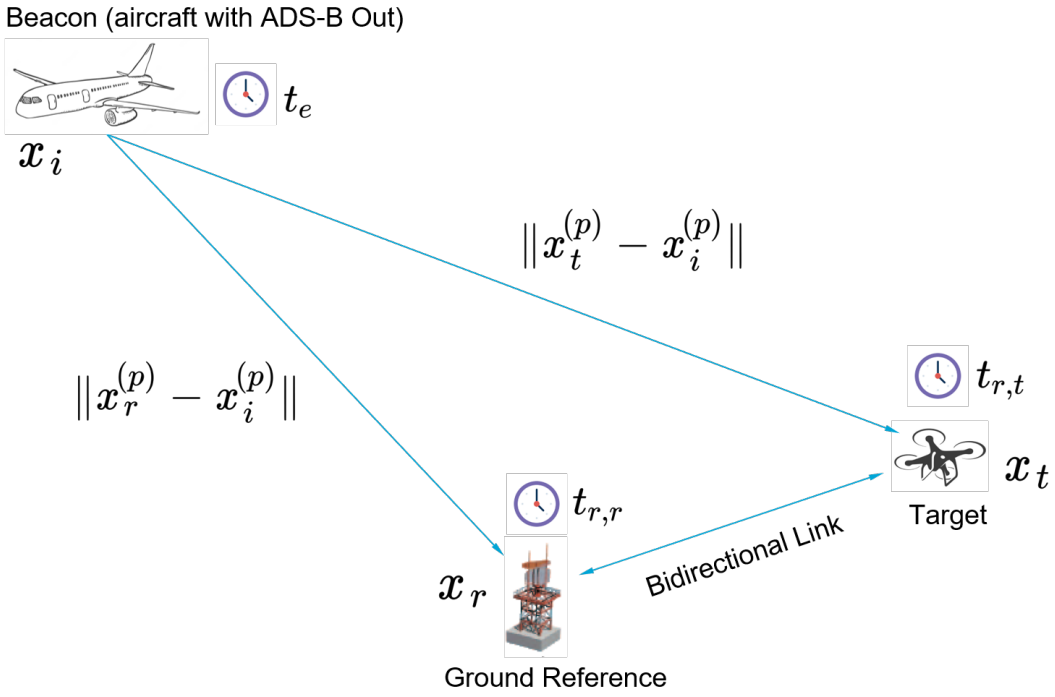

Figure 3.1: The geometric interpretation of SoOp-based TDOA.

a strong assumption. When the i-th beacon ($1 < i < N$) transmits an ADS-B message, time of arrival (TOA) at the reference $t_{r,r}$ is measured and given by

$$t_{r,r} = \frac{\left\| \boldsymbol{x}_r^{(p)} - \boldsymbol{x}_i^{(p)} \right\|}{c} + t_e \tag{3.1}$$

where t_e is the time of transmission at the beacon and radio waves are assumed to propagate with the speed of light c.

Similarly, TOA measurement at the target is measured and given by

$$t_{r,t} = \frac{\left\| \boldsymbol{x}_t^{(p)} - \boldsymbol{x}_i^{(p)} \right\|}{c} + t_e \tag{3.2}$$

where t_e is the time of transmission at the beacon.

Here t_e is unknown for both the target and the reference. To circumvent this, we derive TDOA measurement ρ_i between the target and the reference w.r.t. beacon i instead.

$$\rho_i = t_{r,t} - t_{r,r} + w_i \tag{3.3}$$

where w_i is the measurement noise.

For convenience, we let ρ_i absorb the speed of light c and adjust the magnitude of measurement noise w_i accordingly. Hence, the TDOA measurement equation can be rewritten as

$$\rho_i = \left\| \boldsymbol{x}_t^{(p)} - \boldsymbol{x}_i^{(p)} \right\| - \left\| \boldsymbol{x}_r^{(p)} - \boldsymbol{x}_i^{(p)} \right\| + w_i \tag{3.4}$$

In this TDOA measurement equation, the location of the i-th beacon can be decoded from the ADS-B message, as mentioned in Section2.1. The location of the reference $\boldsymbol{x}_r^{(p)}$ and the time of arrival recorded at the reference $t_{r,r}$ will be sent to the target through the bidirectional communication link depicted in Fig.3.1. The time of arrival $t_{r,t}$ can be obtained at the target. Specific methods of time of arrival measurement particularly for ADS-B signals can be found in [29], which achieve nanosecond-level precision and require only low-cost software-defined radio (SDR) receivers.

For every ADS-B message, a TDOA measurement can be extracted. In order to solve for the location of the target, one needs more than three ($N > 3$) measurements from different beacons. They can be stacked and written as

$$\rho_1 = \left\|\boldsymbol{x}_t^{(p)} - \boldsymbol{x}_1^{(p)}\right\| - \left\|\boldsymbol{x}_r^{(p)} - \boldsymbol{x}_1^{(p)}\right\| + w_1 \tag{3.5}$$

$$\rho_2 = \left\|\boldsymbol{x}_t^{(p)} - \boldsymbol{x}_2^{(p)}\right\| - \left\|\boldsymbol{x}_r^{(p)} - \boldsymbol{x}_2^{(p)}\right\| + w_2 \tag{3.6}$$

$$\vdots$$

$$\rho_N = \left\|\boldsymbol{x}_t^{(p)} - \boldsymbol{x}_N^{(p)}\right\| - \left\|\boldsymbol{x}_r^{(p)} - \boldsymbol{x}_N^{(p)}\right\| + w_N \tag{3.7}$$

This is a nonlinear set of equations in $\boldsymbol{x}_t^{(p)}$.

3.3 Solving SoOp Equations

If the target is able to receive multiple messages simultaneously and generate multiple pairs of TDOA measurements, we can estimate the target's location by solving a set of nonlinear equations iteratively in a fashion similar to solving GNSS pseudorange equations [22].

First, some mathematical manipulation is needed to reformulate the problem, which is shown as follows.

$$d_i = \rho_i + \left\|\boldsymbol{x}_r^{(p)} - \boldsymbol{x}_i^{(p)}\right\| = \left\|\boldsymbol{x}_t^{(p)} - \boldsymbol{x}_i^{(p)}\right\| + w_{\rho,i} \tag{3.8}$$

To solve equations iteratively, one needs an initial value to start. An initial guess of the target's state, $\boldsymbol{x}_t^{(p,0)}$, can obtained from other onboard sensors, say, the inertial measurement unit (IMU). Let us calculate $d_i^{(0)}$ with the known position of the ith beacon $\boldsymbol{x}_i^{(p)}$ and the initial guess $\boldsymbol{x}_t^{(p,0)}$.

$$d_i^{(0)} = \left\|\boldsymbol{x}_t^{(p,0)} - \boldsymbol{x}_i^{(p)}\right\| + w_{\rho,i} \tag{3.9}$$

The difference between the real measurement d_i and predicted $d_i^{(0)}$ is given by

$$\delta d_i = d_i - d_i^{(0)} = \left(\left\|\boldsymbol{x}_t^{(p)} - \boldsymbol{x}_i^{(p)}\right\| + w_{\rho,i}\right) - \left(\left\|\boldsymbol{x}_t^{(p,0)} - \boldsymbol{x}_i^{(p)}\right\| + w_{\rho,i}\right) \tag{3.10}$$

If we rewrite the real position of the target $\boldsymbol{x}_t^{(p)}$ as a combination of the current estimate and an residual error term, which is

$$\boldsymbol{x}_t^{(p)} = \boldsymbol{x}_t^{(p,0)} + \delta\boldsymbol{x}_t^{(p)} \tag{3.11}$$

Then a natural idea is to update the estimate by every iteration and reduce the residual error. Substitute 3.11 into the expression of discrepancy in the real and predicted measurement, we get

$$\delta d_i = \left\| \boldsymbol{x}_t^{(p,0)} + \delta \boldsymbol{x}_t^{(p)} - \boldsymbol{x}_i^{(p)} \right\| - \left\| \boldsymbol{x}_t^{(p,0)} - \boldsymbol{x}_i^{(p)} \right\| \tag{3.12}$$

This is the error equation. We'd like to further linearize this error equation to formulate it as a least squares problem. The linearization is done with respect to the position of the target. It is given by

$$\delta d_i = -\frac{(\boldsymbol{x}_i^{(p)} - \boldsymbol{x}_t^{(p,0)})}{\left\| \boldsymbol{x}_i^{(p)} - \boldsymbol{x}_t^{(p,0)} \right\|} \delta \boldsymbol{x}_t^{(p)} \tag{3.13}$$

Note that the coefficient term in front of the unknown $\delta \boldsymbol{x}_t^{(p)}$ in 3.13 is actually the direction vector from $\boldsymbol{x}_i$ to $\boldsymbol{x}_t$. We denote it by

$$\boldsymbol{u}_{t,i} = \frac{(\boldsymbol{x}_t^{(p,0)} - \boldsymbol{x}_i^{(p)})}{\left\| \boldsymbol{x}_t^{(p,0)} - \boldsymbol{x}_i^{(p)} \right\|} \tag{3.14}$$

We also define $\mathbf{1} = \boldsymbol{u}_{t,i}^T$ which is an 1-by-3 row vector.

If the target observed multiple beacons in proximity, say, 6 beacons ($N = 6$). Multiple TDOA measurements can be stacked as

$$\begin{bmatrix} \delta d_1 \\ \delta d_2 \\ \delta d_3 \\ \delta d_4 \\ \delta d_5 \\ \delta d_6 \end{bmatrix} = \begin{bmatrix} \mathbf{1}_1 \\ \mathbf{1}_2 \\ \mathbf{1}_3 \\ \mathbf{1}_4 \\ \mathbf{1}_5 \\ \mathbf{1}_6 \end{bmatrix} \delta \boldsymbol{x}_t^{(p)} \tag{3.15}$$

This method is called the Newton-Raphson method. It is inherently a method to solve nonlinear equations, but contains a linearization and solves the problem by least squares in every iteration.

Cooperative Navigation of Multiple UAVs

4

In this chapter, the localization problem of multiple UAVs in GNSS-denied environments is explored. In Section4.1, a leader-follower framework for cooperative navigation is proposed based on inter-UAV communication networks. The ADS-B SoOp proposed in Chapter3 is incorporated as an alternative way to provide absolute location information in GNSS-denied environments. We also discuss how this navigation information is shared among multiple UAVs. Under this leader-follower framework, the navigation system for individual UAVs is designed to fuse both shared navigation information and onboard sensor information. Its general architecture and detailed design are presented in Section4.2 and 4.3. Finally, some simulation results are shown in Section4.4 to verify the proposed algorithms.

4.1 Problem Formulation

Suppose there are a group of UAVs deployed in the field. Each of them is equipped with inertial measurement units (IMU), GNSS receivers, and some specific type of aiding sensor intended for APNT. Initially, the UAVs use the primary PNT source, namely the GNSS service, to navigate. After some time, GNSS signals become unavailable due to intentional radio interference. The UAVs then initiate APNT aiding sensors and perform cooperative navigation with the help of the ground station and inter-UAV communication networks.

The cooperative navigation strategy is described as follows. In an inter-UAV, cooperative network, all UAVs involved fall into two categories, leaders or followers. The main differences lie in the role they play in the network, the type of aiding sensors equipped, and their capability. A leader is a UAV that has direct access to absolute position information. Leader UAVs are equipped with ADS-B SoOp receivers and air-to-ground communication devices. Hence, they are capable of exploiting ADS-B SoOp signals to obtain geographic locations with the help of a ground station, which has been introduced in Chapter3. Meanwhile, leader UAVs also have bidirectional communication links to (at least some of) the follower UAVs and share with them leaders' own position estimates. A follower is a UAV that only has direct access to relative position information with respect to some chosen neighbour. Follower UAVs are equipped with two-way ranging (TWR) devices and are capable of inter-UAV communication. They obtain relative positions through TWR module as well as their neighbours' position estimates. With this information they compute their own positions. In other words, the absolute position information flows from the leader to all followers. A chosen neighbour of the follower UAV can either be a leader or a follower itself.

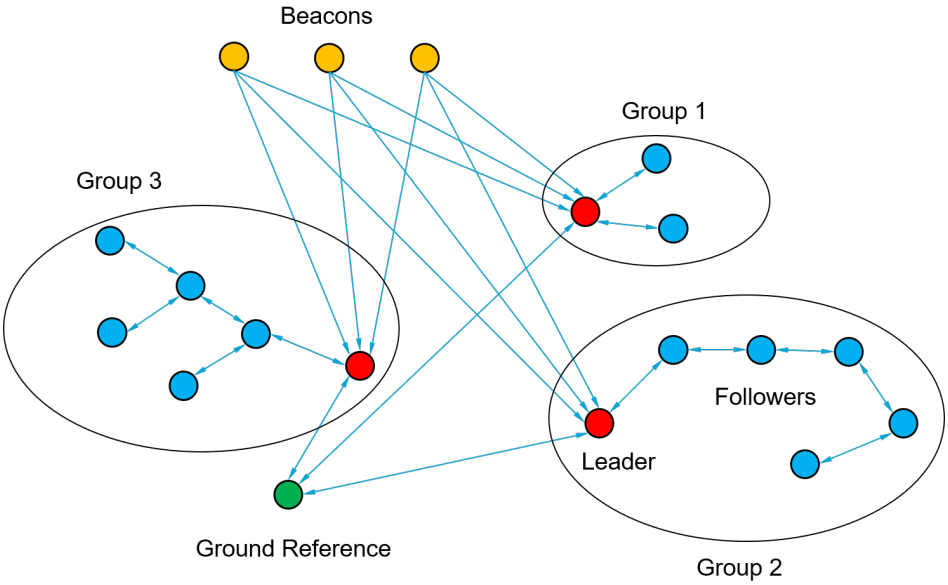

Figure 4.1: The leader-follower network structure of UAVs, beacons, and the ground reference. To emphasize on UAV network configurations, the arrowed lines from beacons to the reference indicating signal transmission are omitted.

From a network perspective, however, neighbours are not arbitrarily chosen for followers. Typical configurations of the inter-UAV network are shown in Fig.4.1. In this figure, all UAVs in operation are divided into three groups. Each group demonstrates a possible network configuration. Within the group boundary of black solid circles, a red mark represents a leader while a blue mark represents a follower. Every blue solid line with arrows on both sides indicate a bidirectional communication link between a pair of UAVs. We observe that

- the minimum connectivity requirement is that all UAVs in the same group be connected;
- a UAV can act as neighbour of multiple other UAVs;
- at least one follower UAV chooses the leader in the network as its neighbour.

In such networks, we further define the distance to the leader for a follower as the number of hops in the network following a shortest path from that particular follower to the leader. If a follower UAV has the distance of h hops, then it is called a D(h) target (UAV). The leader is thus a D(0) target. As long as the capability of communication device permits, multiple targets with the same D(h) value can exist in the network.

We further observe that in order to let absolute position information be used by all targets (directly or indirectly), an order of transmission needs to be designed. It is designed in such a way that absolute position information should always flow from a D($h-1$) target to a D(h) target. Intuitively, the information always propagates from the leader to the "farthest" follower(s) with the largest D(h) value in the network.

In this thesis, the cooperative strategy mentioned above is referred to as the leader-follower strategy. In our case, leaders have access to crucial navigation information

from ADS-B SoOp as well as air-to-ground communication capability, both of which followers lack. A leader is able to navigate as long as the ground station is available, while followers must rely on the leader and cooperation across the network.

The leader-follower strategy is more on the inter-UAV cooperation side. The navigation problem of each individual UAV, however, remains unaddressed. Practically, the location update rate of ADS-B SoOp receivers is low, which makes it unsuitable as the only navigation sensor for small, agile UAVs. It is inherently limited by the broadcast frequency of ADS-B signal sources and the number of simultaneous broadcast during one observation period. For example, the airborne positions of piloted aircraft are broadcast by ADS-B transponders with 2Hz [20]; if there are three groups of beacons alternately broadcasting signals, with four beacons simultaneously broadcasting in each group, the update rate is then 6Hz. This requires 12 beacons in view and a special broadcasting order. With abundant beacons in view, the update rate may be equal to or higher than 2Hz, but it is unlikely to achieve an update rate higher than civilian GNSS receivers (typically < 10Hz). As a result, follower UAVs without SoOp receivers also acquire absolute position information at such a low rate.

The solution to this problem is to incorporate onboard IMU into the navigation system. Typical low-cost micro-electromechanical system (MEMS) IMU has a sampling rate of 100Hz or even higher. It is capable of capturing small motions of UAVs and providing much denser estimates of position or other states. However, the low-cost, consumer-grade IMU has bad long-term stability. Its estimation bias grows unboundedly with time. Therefore, these two sensors have complementary properties. The ADS-B SoOp sensor provides positioning data with bounded errors but at a lower rate, while the IMU has a high update rate and is good at measuring small motions but its output drifts with time. It is then a sensor fusion problem of how to fuse data from the two sensors to achieve a better navigation performance than that of using either one of them.

4.1.1 Updated List of Assumptions

In addition to system assumptions listed in Section3.1.1, we add three more assumptions regarding leaders, followers, and network configuration:

- leaders have direct access to absolute position information and air-to-ground communication capability;
- followers have access to relative position information w.r.t. its chosen neighbour and inter-UAV communication capability;
- the inter-UAV communication network is, topologically, a connected graph;

4.2 Sensor Fusion Architecture

To fuse data from the IMU and the aiding sensor, a loosely-coupled architecture is used, which is shown in Fig.4.2.

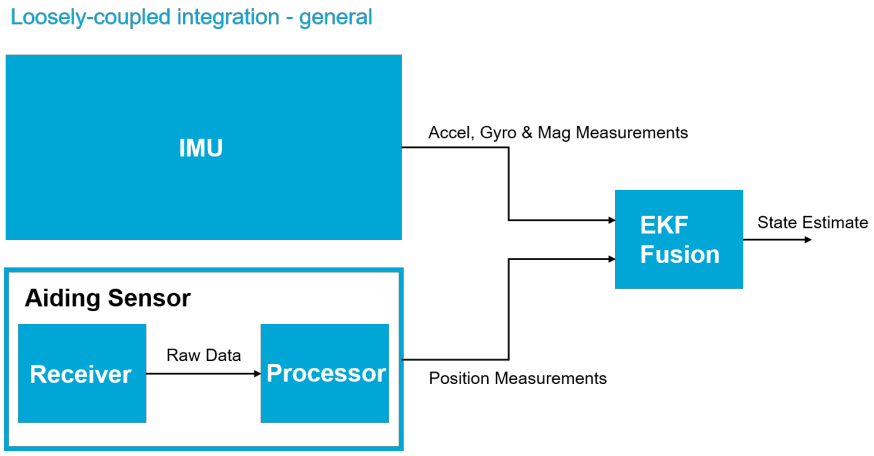

Figure 4.2: The general sensor fusion architecture of all UAVs(targets).

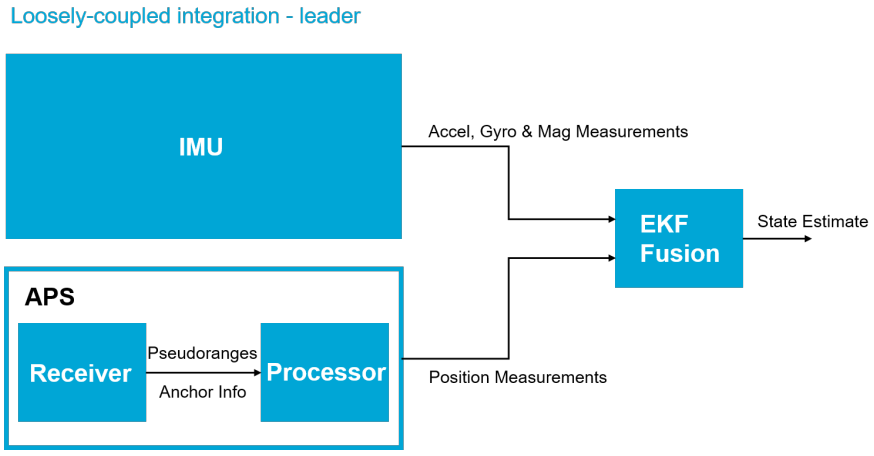

Figure 4.3: The sensor fusion architecture of a "leader" UAV.

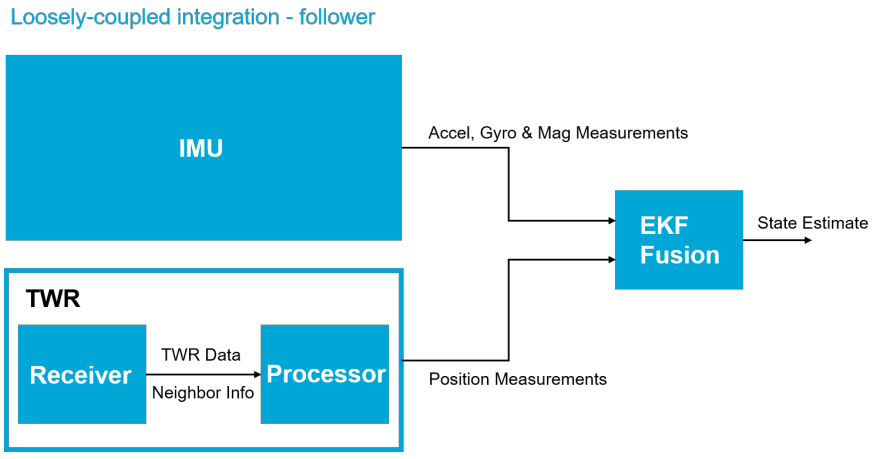

Figure 4.4: The sensor fusion architecture of a "follower" UAV.

An 9-axis IMU provides three-dimensional measurements of linear acceleration (by accelerometer, "Accel"), angular velocity (by gyroscope, "Gyro"), and geomagnetic field vector (by magnetometer, "Mag"). The aiding sensor, without specifying the type for now, just outputs measurements of the platform's positions. The sensor data are then fused by an extended Kalman filter (EKF). Theoretical contents on EKF is presented in Section2.4.

The term "loosely-coupled" refers to the fact that the aiding sensor provides direct state measurements (e.g., three-dimensional position) instead of some raw measurements (e.g., GNSS-like pseudorange and pseudorange rates) which are linked to internal states of the EKF by more complex relations. In the next section, we will see that this architecture simplifies the measurement model design of the fusion filter. Different types of aiding sensors can be easily fused using the same measurement model in the fusion filter.

As mentioned above, the aiding sensor is different for leaders and followers. For a leader UAV, the aiding sensor consists of an ADS-B receiver and a processor. We refer to this module by the name "APS" (ADS-B Positioning by Signal-of-opportunity). The ADS-B receiver extracts time difference of arrival (TDOA) measurements of all available beacons with respect to the ground reference station. With the reference position acquired by air-to-ground communication, the processor is able to estimate the position by solving a set of SoOp measurement equations, as discussed in Chapter 3. Finally, the position estimates from this module are treated as direct state measurements and forwarded to the EKF fusion filter. The workflow is shown in Fig.4.3.

For a follower UAV, the aiding sensor includes a two-way-ranging (TWR) module and a processor for computing positions. The TWR module acquires the position of a chosen neighbour by interrogating that neighbour. Additionally, time of arrival (TOA) recorded at both sides during two-way communication are acquired and direction of arrival (DOA) is estimated. In the signal processor, first the relative position is estimated with TOA and DOA information. Then it is added by the neighbour's position to estimate the position of the follower itself. This is also regarded as direct state measurements and forwarded to the EKF fusion filter. The workflow is shown in Fig.4.4.

4.3 EKF Model Description

4.3.1 Motion Model

In tracking and surveillance applications, an abundant set of motion models have been proposed [30]. People are quite interested in utilizing multiple motion models simultaneously in order to better capture the dynamics of targets [31]. In such multiple model approaches, each model usually corresponds to a specific type of motion.

For self-state estimation tasks, however, if the sampling rate of onboard sensors are high enough, during the sampling interval some simple type of motion can be assumed (e.g., uniform linear motion, uniformly accelerated rectilinear motion). Hence, a generic motion model is preferred. With high sampling rate and a generic motion model, the sophisticated modeling of target's real dynamics can be circumvented and

the navigation algorithm are readily applied to different platforms, whether it is an unmanned aerial vehicle, a rover, or an autonomous ship.

Let us first define the states for the fusion filter. With 9-axis strapdown IMUs, it is possible to simultaneously estimate the orientation, velocity, and position of the platform as well as the local geomagnetic vector. Additionally, it is necessary for consumer-grade IMUs to estimate the sensor bias given its poor long-term stability. All the states are incorporated in a 22-element vector that is given by

$$\boldsymbol{x}_t = [q, \boldsymbol{p}_{NED}^T, \boldsymbol{v}_{NED}^T, \boldsymbol{b}_{\Delta\theta}^T, \boldsymbol{b}_{\Delta v}^T, \boldsymbol{g}_{NED}^T, \boldsymbol{b}_m^T]^T \tag{4.1}$$

where

$$\boldsymbol{p}_{NED} = [p_N, p_E, p_D]^T \tag{4.2}$$
$$\boldsymbol{v}_{NED} = [v_N, v_E, v_D]^T \tag{4.3}$$
$$\boldsymbol{b}_{\Delta\theta} = [b_{\Delta\theta,x}, b_{\Delta\theta,y}, b_{\Delta\theta,z}]^T \tag{4.4}$$
$$\boldsymbol{b}_{\Delta v} = [b_{\Delta v,x}, b_{\Delta v,y}, b_{\Delta v,z}]^T \tag{4.5}$$
$$\boldsymbol{g}_{NED} = [g_N, g_E, g_D]^T \tag{4.6}$$
$$\boldsymbol{b}_m = [b_{m,x}, b_{m,y}, b_{m,z}]^T \tag{4.7}$$
$$\tag{4.8}$$

where q_0, q_1, q_2, and q_3 are four components of a quaternion (see Section2.3) which describes the rotation from the coordinate frame fixed on the current platform (UAV body frame) to the local navigation frame (a North-East-Down frame) in the three-dimensional space; $[p_N, p_E, p_D]^T$ and $[v_N, v_E, v_D]^T$ are three-dimensional position and velocity in the local navigation frame, respectively; $[g_N, g_E, g_D]^T$ is the estimated geomagnetic field vector in the local navigation frame. Furthermore, sensor biases are modeled as additive constant terms. $[b_{\Delta\theta,x}, b_{\Delta\theta,y}, b_{\Delta\theta,z}]^T$ and $[b_{\Delta v,x}, b_{\Delta v,y}, b_{\Delta v,z}]^T$ represent the bias in the angular increment $[\Delta\theta_x, \Delta\theta_y, \Delta\theta_z]^T$ and the velocity increment $[\Delta v_x, \Delta v_y, \Delta v_z]^T$, respectively. The bias in magnetometer readings is modeled as $[b_{m,x}, b_{m,y}, b_{m,z}]^T$.

Please note that the angular and velocity increment are used in the state update of EKF and they are not directly obtained from the gyroscope and the accelerometer. The two sensors measure the angular velocity and the linear acceleration, respectively. Raw outputs are then integrated using the trapezoidal rule

$$\Delta\boldsymbol{\theta}_{raw} = \frac{\Delta T}{2}(\boldsymbol{\omega}_0 + 2\boldsymbol{\omega}_1 + \ldots + 2\boldsymbol{\omega}_{M-1} + 2\boldsymbol{\omega}_M) \tag{4.9}$$
$$\Delta\boldsymbol{v}_{raw} = \frac{\Delta T}{2}(\boldsymbol{a}_0 + 2\boldsymbol{a}_1 + \ldots + 2\boldsymbol{a}_{M-1} + 2\boldsymbol{a}_M) \tag{4.10}$$
$$\tag{4.11}$$

where $\Delta\boldsymbol{\theta}$, $\Delta\boldsymbol{v} \in \mathcal{R}^3$ are angular and velocity increments; ΔT is the sampling interval between time instant $k-1$ and k; $\boldsymbol{\omega}_i (i = 0, 1, 2, ..., M) \in \mathcal{R}^3$ is the raw angular velocity data from the gyroscope; $\boldsymbol{a}_i (i = 0, 1, 2, ..., M) \in \mathcal{R}^3$ is the raw linear acceleration data from the accelerometer; $M \geq 1$ is the number of sampling intervals. Please note that all these quantities are measured and computed in the body frame of the UAV.

With angular and velocity increments obtained, now we are ready to formulate the state update. First, the increments are subtracted by the biases $\boldsymbol{b}_{\Delta\theta} = [b_{\Delta\theta,x}, b_{\Delta\theta,y}, b_{\Delta\theta,z}]^T$ and $\boldsymbol{b}_{\Delta v} = [b_{\Delta v,x}, b_{\Delta v,y}, b_{\Delta v,z}]^T$. Next, let us assume the orientation change during sampling interval, which is sufficiently small, is approximated by $(\Delta\boldsymbol{\theta}_{raw} - \boldsymbol{b}_{\Delta\theta}) \in \mathcal{R}^3$. It is converted to a quaternion denoted by $q' = [q'_0, q'_1, q'_2, q'_3]^T$. According to Section2.3, the updated orientation is given by

$$q_k = q_{k-1} \otimes q' \tag{4.12}$$

where the orientation q_{k-1} at the last time instant $k-1$ is updated by multiplying q' to obtain q_k. Hence, the transition matrix $\boldsymbol{F}_q$ is given by the Jacobian matrix taken with respect to the states involved. Note that for this particular equation, not only the orientation are involved but also the bias of angular increments. A detailed derivation of $\boldsymbol{F}_q$ can be found in [32].

Since the velocity increment $\Delta\boldsymbol{v} = (\Delta\boldsymbol{v}_{raw} - \boldsymbol{b}_{\Delta v}) \in \mathcal{R}^3$ is measured in the body frame of the UAV, it is necessary to convert it to the local navigation frame, which can be written as

$$\Delta\boldsymbol{v}_{NED} = q_{k-1} \otimes \Delta\boldsymbol{v} \otimes q^*_{k-1} \tag{4.13}$$

where $\Delta\boldsymbol{v}_{NED}$ is the velocity increment in the local navigation frame. Hence, the velocity update equation is

$$\boldsymbol{v}_{NED,k} = \boldsymbol{v}_{NED,k-1} + \Delta\boldsymbol{v}_{NED} + \boldsymbol{a}_{g,NED} \cdot \Delta T \tag{4.14}$$

where the updated velocity vector at time instant k is $\boldsymbol{v}_{NED,k} \in \mathcal{R}^3$. Apart from the velocity increment, the local gravitational acceleration $\boldsymbol{a}_{g,NED}$ also has an influence on the velocity. The state transition matrix $\boldsymbol{F}_v$ is obtained by finding the corresponding Jacobian matrix, which is described in detail in [32].

The position update assumes a simple uniform linear motion and is given by

$$\boldsymbol{p}_{NED,k} = \boldsymbol{p}_{NED,k-1} + \boldsymbol{v}_{NED,k-1} \cdot \Delta T \tag{4.15}$$

where $\boldsymbol{p}_{NED,k} \in \mathcal{R}^3$ and $\boldsymbol{p}_{NED,k-1} \in \mathcal{R}^3$ are positions expressed in the local navigation frame (North-East-Down) at time instance k and $k-1$ respectively. The corresponding state transition matrix $\boldsymbol{F}_p$ is given by

$$\boldsymbol{F}_p = \begin{bmatrix} \boldsymbol{0}_{3\times4} & \boldsymbol{I}_{3\times3} & \Delta T\boldsymbol{I}_{3\times3} & \boldsymbol{0}_{3\times6} & \boldsymbol{0}_{3\times3} & \boldsymbol{0}_{3\times3} \end{bmatrix} \tag{4.16}$$

The geomagnetic field vector has the following transition model

$$\boldsymbol{g}_{NED,k} = \boldsymbol{I}_{3\times3}\, \boldsymbol{g}_{NED,k-1} + \boldsymbol{w}_{geo,k} \tag{4.17}$$

where $\boldsymbol{g}_{NED} = [g_N, g_E, g_D]^T$ is a part of the state vector that represents the local geomagnetic vector in the local navigation frame; the corresponding transition matrix is set as an identity and possible variation is modeled in the noise term $\boldsymbol{w}_{geo}$. The complete state transition matrix $\boldsymbol{F}_{geo}$ is given by

$$\boldsymbol{F}_{geo} = \begin{bmatrix} \boldsymbol{0}_{3\times4} & \boldsymbol{0}_{3\times3} & \boldsymbol{0}_{3\times3} & \boldsymbol{0}_{3\times6} & \boldsymbol{I}_{3\times3} & \boldsymbol{0}_{3\times3} \end{bmatrix} \tag{4.18}$$

It is worth noting that sensor biases often vary slowly in time. In other words, if we include a slowly changing bias term in the process noise, the probability distribution of the process noise will be a normal distribution with a nontrivial, time-varying mean, which violates the assumptions of the Kalman filter. Hence, it makes more sense to incorporate sensor biases in the state vector.

In our application, time-varying biases of the angular increment, the velocity increment, and the magnetometer readings have the corresponding state transition model

$$\begin{bmatrix} \boldsymbol{b}_{\Delta\theta} \\ \boldsymbol{b}_{\Delta v} \\ \boldsymbol{b}_m \end{bmatrix}_k = \boldsymbol{I}_{9\times 9} \begin{bmatrix} \boldsymbol{b}_{\Delta\theta} \\ \boldsymbol{b}_{\Delta v} \\ \boldsymbol{b}_m \end{bmatrix}_{k-1} + \begin{bmatrix} \boldsymbol{w}_{\Delta\boldsymbol{\theta}} \\ \boldsymbol{w}_{\Delta\boldsymbol{v}} \\ \boldsymbol{w}_m \end{bmatrix}_k \tag{4.19}$$

where $\boldsymbol{I}_{9\times 9}$ is an 9-by-9 identity matrix and $\boldsymbol{w}_{\Delta\boldsymbol{\theta}} \in \mathcal{R}^3$, $\boldsymbol{w}_{\Delta\boldsymbol{v}} \in \mathcal{R}^3$, and $\boldsymbol{w}_m \in \mathcal{R}^3$ are random variables representing process noise. Setting the transition matrix as identity, we model the sensor biases as random walk processes using additive white Gaussian noise. It can be considered as reflecting the stability of the sensor biases. The complete state transition matrix for all the sensor bias terms is then given by

$$\boldsymbol{F}_{bias} = \begin{bmatrix} \boldsymbol{F}_{b1} \\ \boldsymbol{F}_{b2} \end{bmatrix} \tag{4.20}$$

where $\boldsymbol{F}_{b1} \in \mathcal{R}^{6\times 22}$ models the state transition of the bias in angular and velocity increments; $\boldsymbol{F}_{b2} \in \mathcal{R}^{3\times 22}$ models the state transition of the magnetometer bias. They are defined as

$$\boldsymbol{F}_{b1} = \begin{bmatrix} \boldsymbol{0}_{6\times 4} & \boldsymbol{0}_{6\times 3} & \boldsymbol{0}_{6\times 3} & \boldsymbol{I}_{6\times 6} & \boldsymbol{0}_{6\times 3} & \boldsymbol{0}_{6\times 3} \end{bmatrix} \tag{4.21}$$

$$\boldsymbol{F}_{b2} = \begin{bmatrix} \boldsymbol{0}_{3\times 4} & \boldsymbol{0}_{3\times 3} & \boldsymbol{0}_{3\times 3} & \boldsymbol{0}_{3\times 6} & \boldsymbol{0}_{3\times 3} & \boldsymbol{I}_{3\times 3} \end{bmatrix} \tag{4.22}$$

Finally, the state transition matrix $\boldsymbol{F}_t$ for the full state vector $\boldsymbol{x}_t$ is given by

$$\boldsymbol{F}_t = \begin{bmatrix} \boldsymbol{F}_q \\ \boldsymbol{F}_p \\ \boldsymbol{F}_v \\ \boldsymbol{F}_{b1} \\ \boldsymbol{F}_{geo} \\ \boldsymbol{F}_{b2} \end{bmatrix} \tag{4.23}$$

4.3.2 Measurement Model

For the loosely-coupled architecture, direct state measurements (i.e., position measurements) of the target are available to the fusion filter, so the measurement model is given by

$$\begin{bmatrix} z_{loc,N} \\ z_{loc,E} \\ z_{loc,D} \end{bmatrix}_k = \boldsymbol{I}_{3\times 3} \begin{bmatrix} p_N \\ p_E \\ p_D \end{bmatrix}_k + \boldsymbol{v}_{loc,k} \tag{4.24}$$

Other states irrelevant to the measurement model are hence not included. The corresponding entries of these irrelevant states in the measurement matrix are filled

with zeros. The complete measurement matrix $\boldsymbol{H}_t$, conforming to the definition of the state vector in Section4.3.1, is written as

$$\boldsymbol{H}_t = \begin{bmatrix} \mathbf{0}_{3\times4} & \boldsymbol{I}_{3\times3} & \mathbf{0}_{3\times3} & \mathbf{0}_{3\times6} & \mathbf{0}_{3\times3} & \mathbf{0}_{3\times3} \end{bmatrix} \tag{4.25}$$

Practically, both the APS and the TWR module will output locations in geographic coordinates. Thus, it is useful to convert the longitudes, latitudes, and altitudes to coordinates under the North-East-Down local navigation frame.

4.3.3 Pseudo Code

Finally, the pseudo code of the EKF-based sensor fusion algorithm is presented as follows.

Algorithm 2 The EKF-based sensor fusion algorithm

Input: $\boldsymbol{x}_{t,0}$, initial state
$\boldsymbol{P}_{t,0}$, initial uncertainty
$\boldsymbol{Q}_k$, $\boldsymbol{R}_k$ ($k \in \{1, 2, 3, .., K\}$), noise covariance matrices
$\boldsymbol{z}_{loc,k}$, position measurement
Output: $\boldsymbol{x}_{t,k}$, state estimate
$\boldsymbol{P}_{t,k}$, posterior covariance
$\boldsymbol{K}_k$ ($k \in \{1, 2, 3, .., K\}$), Kalman gain

Begin
  Initialize $\boldsymbol{x}_{t,0}$ and $\boldsymbol{P}_{t,0}$ with initial states (e.g., orientation, position, velocity, bias).
  For $k = 1$ to K **do**
    $\tilde{\boldsymbol{x}}_{t,k} = f(\boldsymbol{x}_{t,k-1})$ ▷ State prediction using IMU data
    $\tilde{\boldsymbol{P}}_{t,k} = \boldsymbol{F}_t \boldsymbol{P}_{t,k-1} \boldsymbol{F}_t^T + \boldsymbol{Q}_{k-1}$
    If $\boldsymbol{z}_{loc,k}$ is available
      $\boldsymbol{K}_k = \tilde{\boldsymbol{P}}_{t,k} \boldsymbol{H}_t^T (\boldsymbol{H}_t \tilde{\boldsymbol{P}}_{t,k} \boldsymbol{H}_t^T + \boldsymbol{R}_k)^{-1}$
      $\boldsymbol{x}_{t,k} = \tilde{\boldsymbol{x}}_{t,k} + \boldsymbol{K}_k (\boldsymbol{z}_{loc,k} - g(\tilde{\boldsymbol{x}}_{t,k}))$ ▷ State correction using position data
      $\boldsymbol{P}_{t,k} = (\boldsymbol{I} - \boldsymbol{K}_k \boldsymbol{H}_t) \tilde{\boldsymbol{P}}_{t,k}$
  end
end

4.4 Simulations

4.4.1 Simulation Setup

In this section, simulation results of multiple UAV cooperative localization are presented. The most important assumption, as mentioned in Section4.1, is that all UAVs involved in cooperative navigation as well as the ground reference station are *perfectly* synchronized. We further assume the TWR module introduce very small errors in relative positioning. Asynchronous clocks will introduce new errors in both SoOp-based localization and relative positioning. This will be discussed in detail and tackled in the next chapter.

There are other important simulation parameters listed below. UAVs are equipped with consumer-grade IMUs with typical update rate, measurement range, resolution, and noise parameters. The UAVs are assumed to operate in areas with dense air traffic, hence eight beacons are used in simulation. The trajectories of beacons are designed to mimic that of cruising commercial airplanes, with similar altitude and ground speed. According to the implementation standard of the ADS-B system, the airborne position broadcast rate is 2Hz, leading to a similar low update rate of ADS-B sensors on UAVs. Finally, the standard deviation of beacon locations is 60 meters. According to [27], 95% of the analyzed flights show a cross-track accuracy better than 51.83 meters (0.03 NM), which can be considered as an approximation of the standard deviation value $\sigma_{b,position}$. In [33] researchers conclude that 53% of the aircraft they observe broadcast airborne position reports with a horizontal protection limit (HPL) of 0.1NM, which indicates that there is a probability of 95% that an aircraft is actually in the circular area defined with the reported location as the center and the HPL value as the radius. This is similar to the three-sigma rule for the Gaussian distribution. Thus, we obtain an approximate of $\sigma_{b,position} = 0.033NM$. Key simulation parameters are listed in the table below.

Table 4.1: Key simulation parameters

Simulation parameter	Value
Total simulation time(s)	70
Number of deployed UAVs	5
Number of ground stations	1
IMU sampling rate(Hz)	100
SoOp sensor update rate(Hz)	2
SoOp beacon number	8
SoOp beacon position standard deviation(m)	60
SoOp measurement noise standard deviation(m)	1×10^{-2}
TWR measurement noise standard deviation(m)	0.5
Number of Monte Carlo runs	50

A baseline simulation is first performed using the parameter values listed above. Furthermore, we vary different parameters individually and perform corresponding experiments to analyze the influences of the following factors on the navigation performance:

- localization using only SoOp versus using both IMU and SoOp;
- the number of available beacons (4, 6, and 8 beacons);
- the position uncertainty of available beacons (60m, 180m);
- the network topology of UAVs (shown in Fig.4.5).

4.4.2 Multi-UAV Simulation Results

In our simulation, there are five UAVs deployed in an area of 3500m $\times$ 2000m $\times$ 100m. A ground reference is also deployed at the location $[10, 20, 10]$(m). The pairwise

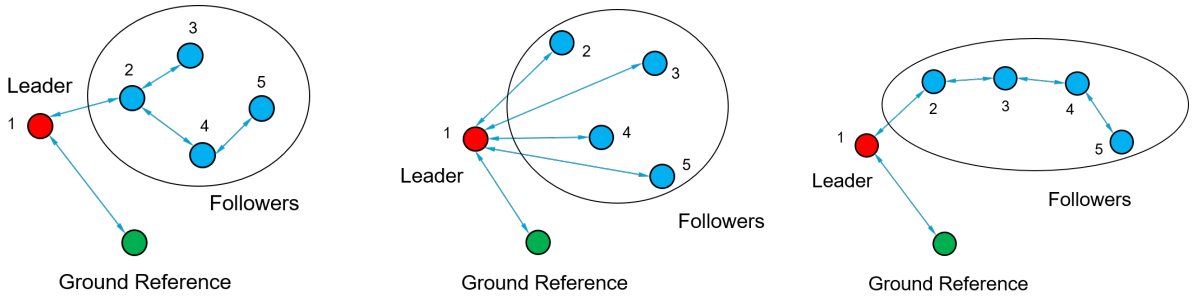

(a) Configuration 1 (b) Configuration 2 (c) Configuration 3

Figure 4.5: Different configurations of UAV networks, including a ground reference.

distances of these UAVs vary from hundreds of to over one thousand meters. Typical wireless technologies using ISM (industrial, scientific and medical) bands (e.g., LoRa, APRS) are able to provide robust connection at this range. Hence the proposed UAV network is feasible.

The trajectories of eight beacons are presented in Fig.4.6. These beacons are a few kilometers away from the area where UAVs are deployed. Their typical ground speed is over 200 knots and typical altitude is above 6000 meters, which are designed to mimic cruising commercial airplanes. A rectangular shape area is bounded by black solid lines, within which UAVs are deployed. The trajectories of five UAVs are presented in Fig.4.7. From the figure we can see that these trajectories contain rich maneuvers. They are selected from the MidAir data set of small, high agility drones [34].

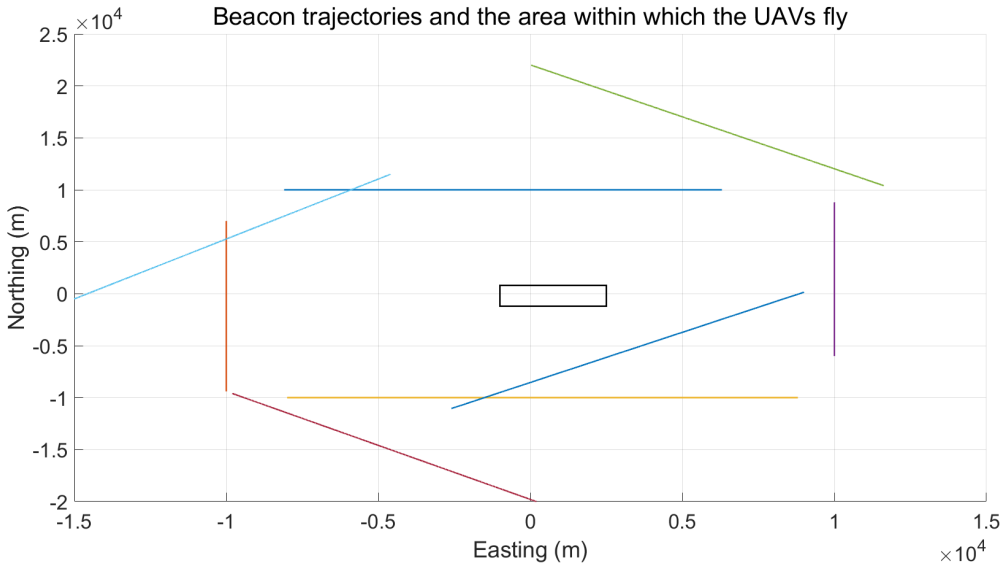

Figure 4.6: Trajectories of beacons and the UAV deployment area

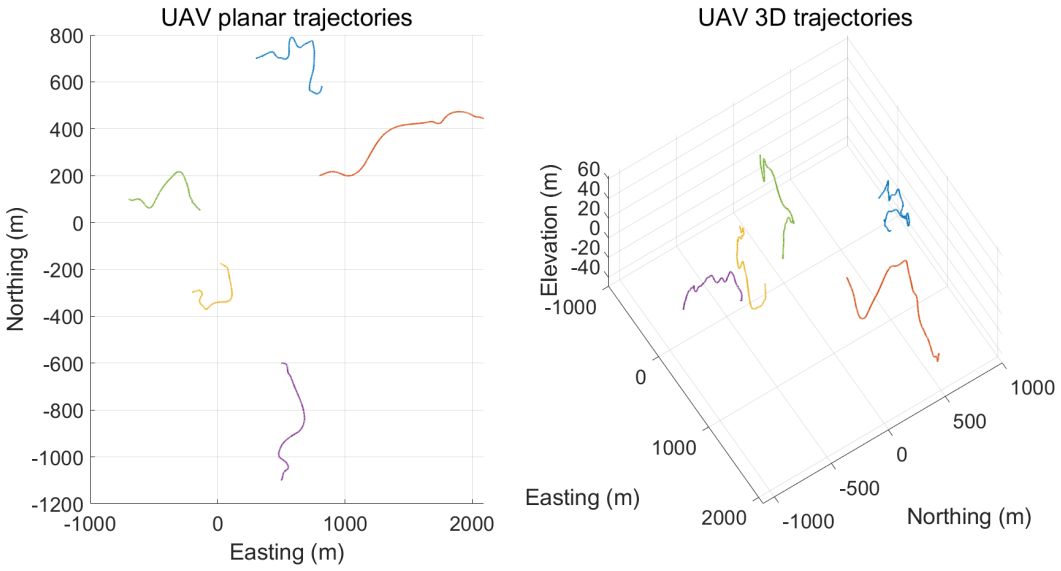

Figure 4.7: Trajectories of UAVs

4.4.3 Baseline Simulation

In this subsection, we present the Monte Carlo simulation results using the parameter values listed in Table4.1. To give an intuition, the estimated trajectory of one of the UAVs are plotted in Fig.4.8. The corresponding estimation error plots of its orientation, position, and velocity are presented in Fig.4.9. The complete results of all five UAVs are presented in Table4.2, 4.3, 4.4, and 4.5. To quantify the performance of the proposed algorithms, three different metrics are used, namely the Averaged Mean Square Error (AMSE), the Root Mean Square Error (RMSE), and the Mean Absolute Error (MAE). They are computed as

$$\mathrm{AMSE}(\hat{\boldsymbol{v}}, \boldsymbol{v}) = N_{exp}^{-1} \sum_{n=1}^{N_{exp}} \|\hat{\boldsymbol{v}} - \boldsymbol{v}\|^2 , \tag{4.26}$$

$$\mathrm{RMSE}(\hat{\boldsymbol{v}}, \boldsymbol{v}) = \sqrt{N_{exp}^{-1} \sum_{n=1}^{N_{exp}} \|\hat{\boldsymbol{v}} - \boldsymbol{v}\|^2}, \tag{4.27}$$

$$\mathrm{MAE}(\hat{\boldsymbol{v}}, \boldsymbol{v}) = N_{exp}^{-1} \sum_{n=1}^{N_{exp}} \|\hat{\boldsymbol{v}} - \boldsymbol{v}\| . \tag{4.28}$$

where N_{exp} is number of experiments conducted; $\hat{\boldsymbol{v}}$ is the obtained estimate; $\boldsymbol{v}$ is the unknown vector to be estimated. Since we compute these three metrics for a range of different quantities with different dimensions, the dimensions of $\hat{\boldsymbol{v}}$ and $\boldsymbol{v}$ are omitted here.

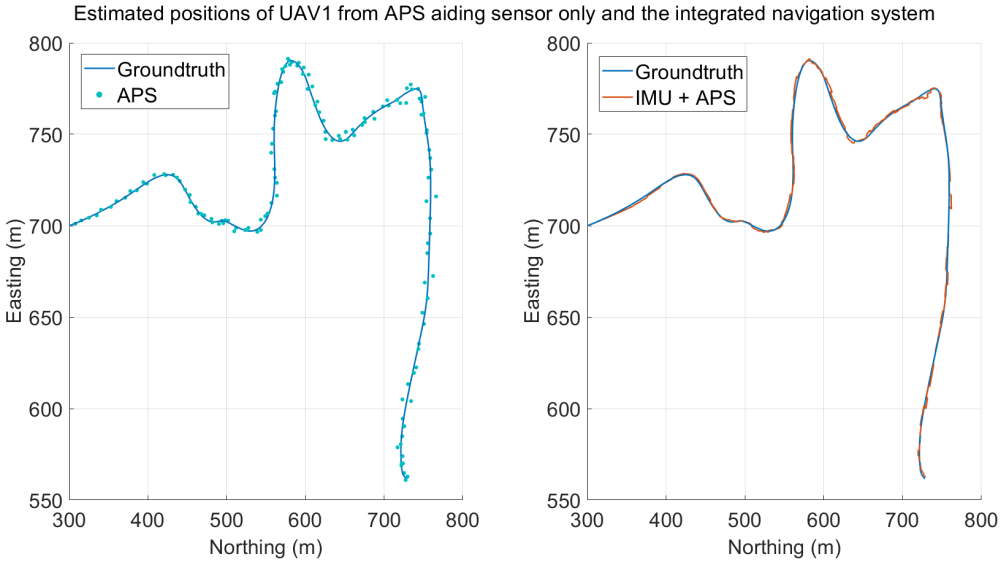

Figure 4.8: Baseline simulation: UAV 1 estimated positions

As seen in the left of Fig.4.8, position estimates from APS are quite sparse compared with the groundtruth trajectory. This is due to the low broadcast rate of ADS-B airborne position reports of beacons. Apparently, these sparse estimates are not adequate for UAV navigation. Hence, it is necessary to also incorporate the IMU. During the update interval of ADS-B SoOp, the fusion filter performs dead reckoning using IMU data. Position estimates provided by ADS-B SoOp are seen as measurements for the correction update of EKF. Note that although ADS-B SoOp has an update rate even lower than that of typical civilian GNSS receivers (5-10Hz), we still managed to use it as navigation aiding source in the proposed algorithm.

Incorporating the IMU not only gives much denser state estimates but also more accurate ones. Comparing the estimation errors in Table4.3 and 4.4, it is observed that the proposed sensor fusion algorithm improve the overall navigation performance, reducing more than 50% of the errors. Furthermore, with IMU data more states such as the orientation and the velocity can be estimated.

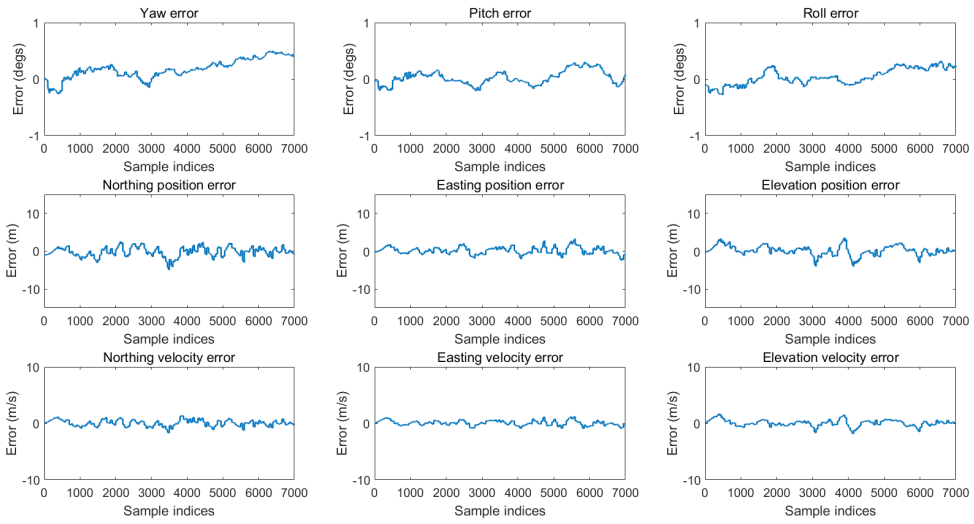

Figure 4.9: Baseline simulation: UAV 1 tracking errors

Table 4.2: Baseline simulation: orientation tracking performance (APS + IMU)

UAV ID	AMSE(degs^2)	RMSE(degs)	MAE(degs)
1	0.0551	0.2348	0.2000
2	0.0525	0.2290	0.1967
3	0.1650	0.4063	0.3645
4	0.2471	0.4971	0.4379
5	0.0547	0.2339	0.2060

Table 4.3: Baseline simulation: position tracking performance (APS only)

UAV ID	AMSE(m^2)	RMSE(m)	MAE(m)
1	4.28	2.05	1.62
2	4.56	2.11	1.67
3	4.84	2.18	1.72
4	4.83	2.18	1.73
5	5.07	2.24	1.77

Table 4.4: Baseline simulation: position tracking performance (APS + IMU)

UAV ID	AMSE(m^2)	RMSE(m)	MAE(m)
1	1.71	1.30	1.03
2	1.83	1.34	1.07
3	1.91	1.37	1.09
4	1.88	1.36	1.08
5	2.03	1.42	1.12

Table 4.5: Baseline simulation: velocity tracking performance (APS + IMU)

UAV ID	AMSE(m^2/s^2)	RMSE(m/s)	MAE(m/s)
1	0.33	0.57	0.45
2	0.36	0.60	0.47
3	0.36	0.59	0.48
4	0.36	0.60	0.49
5	0.39	0.62	0.50

4.4.4 Simulation with Varying Number of Beacons

We now look at the effects of varying number of available beacons. Experiments are performed in the case of four, six, and eight beacons in view. The estimated trajectories are shown in Fig.4.10. The blue line indicates the groundtruth trajectory, while the red, yellow, and purple lines represent estimated trajectories with four, six, and eight beacons respectively.

As the number of available beacons increases, the tracking performance is improved for each of the UAVs. If we look at Fig.4.10, the estimated trajectory becomes smoother as well as more accurate as signals from more beacons are exploited. The zigzag patterns of the trajectories indicate drift of dead reckoning results and corrections using ADS-B SoOp data. Although only the performance of position estimation is analyzed, similar conclusions on the tracking performance of other states can be drawn.

Furthermore, here we only examined the case of four, six, and eight beacons. For cases with less than three available beacons, the system will not work at all because it is a loosely-coupled architecture and the ADS-B SoOp data processing is independent from the fusion filter. The independent SoOp-based TDOA processing requires three or more beacons to give an unambiguous estimate. Hence, the proposed algorithm works under the condition that there is sufficient amount of live air traffic in proximity and at least three or more beacons are in view.

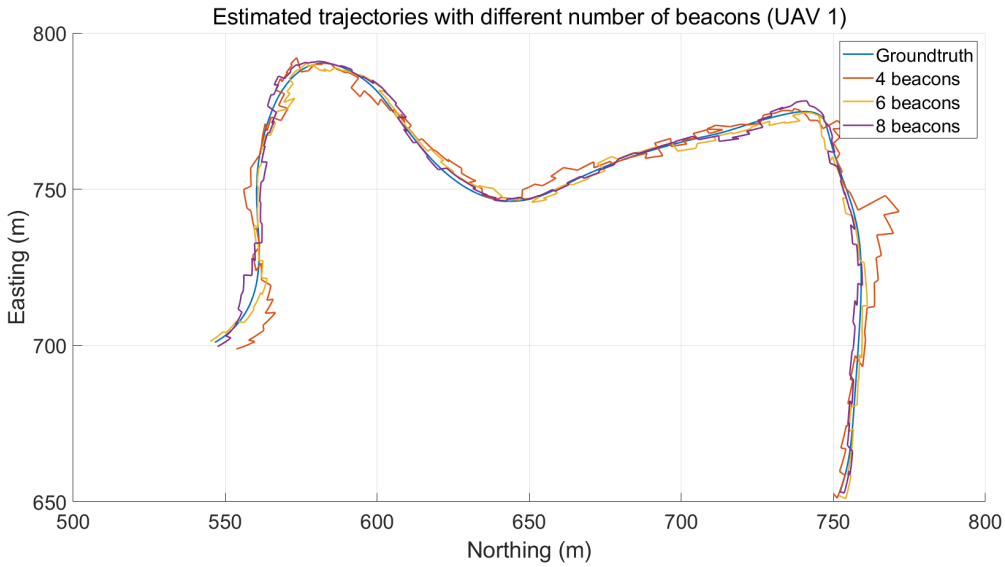

Figure 4.10: Comparison of estimated trajectories of UAV 1

4.4.5 Simulation with Increased Beacon Uncertainty

The influence of beacon uncertainty is also examined. We model the beacon position error (the discrepancy between the reported position through ADS-B and the actual position) as a random error governed by a zero-mean Gaussian distribution, with its standard deviation σ_{b_error}. Monte Carlo experiments are conducted w.r.t. $\sigma_{b\_error} =$ 180m. The simulation results are presented in Table4.6, 4.7, and 4.8. They can be compared with that of the baseline simulation with $\sigma_{b_error} = 60$m.

The tracking performance of all the states degrades as the beacon uncertainty increases. For ADS-B SoOp localization, one disadvantage is that the accuracy of reported beacon positions depend on the performance of civil aviation surveillance technology and infrastructure. Currently, which in most cases provides an accuracy of several tens of meters. This is far less accurate than that of satellite reported positions (normally $<$ 1m [35]). However, as aviation surveillance technology advances, the performance of ADS-B SoOp will benefit from it.

Table 4.6: Simulation with increased beacon uncertainty: orientation tracking performance (APS + IMU)

UAV ID	AMSE(degs^2)	RMSE(degs)	MAE(degs)
1	0.0679	0.2605	0.2212
2	0.0602	0.2453	0.2104
3	0.1625	0.4032	0.3566
4	0.2736	0.5230	0.4594
5	0.0560	0.2366	0.2089

Table 4.7: Simulation with increased beacon uncertainty: position tracking performance (APS + IMU)

UAV ID	AMSE(m^2)	RMSE(m)	MAE(m)
1	14.71	3.79	2.94
2	14.88	3.81	2.96
3	14.80	3.80	2.95
4	14.83	3.81	2.95
5	15.05	3.84	2.98

Table 4.8: Simulation with increased beacon uncertainty: velocity tracking performance (APS + IMU)

UAV ID	AMSE(m^2/s^2)	RMSE(m/s)	MAE(m/s)
1	2.64	1.61	1.26
2	2.69	1.62	1.27
3	2.65	1.61	1.26
4	2.66	1.61	1.26
5	2.70	1.63	1.27

4.4.6 Simulation with Different Network Configurations

Now we turn to the influences of different UAV network configurations. Monte Carlo experiments are conducted with three different configurations shown in Fig.4.5. The results of the first configuration in Fig.4.5a have been presented in Section4.4.3. The results of the other two configurations are presented in Table4.9, 4.10, 4.11 in Section4.4.6.1 and Table4.12, 4.13, 4.14 in Section4.4.6.2, respectively.

First, we observe that the algorithm works as long as the inter-UAV network is topologically a connected graph. Second, difference in network topology has an influence on the tracking performance of individual UAVs. It is observed that for followers with the same D(h) value defined in Section4.1 or in the same "layer" of the network from a leader-centered perspective, similar tracking performance is achieved. Meanwhile, the tracking performance of followers degrades as their D(h) UAV increases. This observation can guide the grouping of a large swarm of UAVs doing cooperative localization. The required localization performance will set a lower bound in accuracy as well as the largest D(h) value that can exist in a network(group), which is a subset of the UAV swarm. For a large swarm of UAVs, it is better to divide them into multiple smaller groups and assign multiple leaders. Meanwhile, multiple leaders will impose a burden on the service capacity of the ground station. Hence, trade-off is needed. An "optimal" assigning strategy and network structure may be of interest in this context.

4.4.6.1 Network Configuration 2

Table 4.9: Simulation of configuration 2: orientation tracking performance (APS + IMU)

UAV ID	AMSE($degs^2$)	RMSE(degs)	MAE(degs)
1	0.0538	0.2320	0.2022
2	0.0630	0.2510	0.2151
3	0.1419	0.3767	0.3340
4	0.2569	0.5068	0.4502
5	0.0619	0.2489	0.2219

Table 4.10: Simulation of configuration 2: position tracking performance (APS + IMU)

UAV ID	AMSE(m^2)	RMSE(m)	MAE(m)
1	1.66	1.28	1.01
2	1.78	1.32	1.05
3	1.77	1.32	1.05
4	1.75	1.31	1.04
5	1.79	1.33	1.05

Table 4.11: Simulation of configuration 2: velocity tracking performance (APS + IMU)

UAV ID	AMSE(m^2/s^2)	RMSE(m/s)	MAE(m/s)
1	0.33	0.57	0.45
2	0.35	0.59	0.47
3	0.34	0.58	0.46
4	0.34	0.58	0.46
5	0.34	0.58	0.47

4.4.6.2 Network Configuration 3

Table 4.12: Simulation of configuration 3: orientation tracking performance (APS + IMU)

UAV ID	AMSE($degs^2$)	RMSE(degs)	MAE(degs)
1	0.0598	0.2446	0.2118
2	0.0537	0.2317	0.2006
3	0.1766	0.4202	0.3662
4	0.2933	0.5416	0.4876
5	0.0535	0.2312	0.2027

Table 4.13: Simulation of configuration 3: position tracking performance (APS + IMU)

UAV ID	AMSE(m^2)	RMSE(m)	MAE(m)
1	1.70	1.29	1.02
2	1.80	1.34	1.06
3	1.89	1.37	1.09
4	1.96	1.39	1.10
5	2.11	1.45	1.15

Table 4.14: Simulation of configuration 3: velocity tracking performance (APS + IMU)

UAV ID	AMSE(m^2/s^2)	RMSE(m/s)	MAE(m/s)
1	0.33	0.57	0.45
2	0.35	0.59	0.47
3	0.36	0.60	0.48
4	0.38	0.61	0.49
5	0.40	0.63	0.51

Joint Relative Positioning and Synchronization

5

In this chapter, the relative positioning as well as the synchronization problem of the inter-UAV network are addressed. As mentioned in Chapter4, the relative positions between each pair of UAVs with a direct communication link need to be estimated. This information is essential for cooperative localization. Since we use the two-way ranging (TWR) method, synchronization between each pair of UAVs is required. Furthermore, in order to use ADS-B SoOp, UAVs need to be synchronized to the ground station as well.

To tackle these problems, a joint relative ranging and synchronization algorithm from [36] is applied. First, an affine model is used to approximate the behaviour of local asynchronous clocks. Second, a polynomial model is used to approximate the time-varying relative range between two UAVs. The mobile pairwise least squares (MPLS) from [36] is performed on every pairwise communication link to jointly solve the ranging and synchronization problem. We further incorporate direction of arrival information with respect to the UAV platform to obtain relative positions. Finally, simulation results show that 1) MPLS converge on the proposed inter-UAV network without increasing connectivity compared to that in Chapter4; 2) the proposed cooperative navigation strategy, with joint relative positioning and synchronization incorporated, is robust against asynchronous clocks of UAVs and the ground station.

5.1 Asynchronous Clocks and Affine Clock Model

In chapter 4, all derivations are based on the idealized assumption that all targets, beacons, and references are synchronized. However, to work with real-world systems, it is more practical to assume that all vehicles involved run their own local clocks and they are not necessarily synchronized. The errors originated from asynchronous clocks will plague the measurements of ADS-B SoOp as well as TWR relative positioning. For example, the typical skew of low-cost oven-controlled crystal oscillators (OCXO) or temperature compensated crystal oscillators (TCXO) ranges from 10^{-11} to 10^{-6} [37]. It contributes a timing error of up to 86.4ms during one day. Even in a period of 100ms, considering the propagation speed of light, this will, in the worst case, add an error of 60 meters to the pseudorange measurement.

If there is a ground reference, the UAVs are able to synchronize to it. Furthermore, if the ground reference itself is quipped with a clock precise enough with respect to some "true" time, say, the GNSS reference time, the UAVs will simultaneously get timing service. However, as seen in Chapter4, only leader UAVs have bidirectional communication with the ground reference. It is then a problem how follower UAVs can also be synchronized to the ground reference without direct communication links.

Let's start with the simplest case where only two UAVs are involved. If we define a

standard time frame as the "true" time, local clocks, due to hardware imperfections and environment temperature, vary nonlinearly with respect to the true time. Nevertheless, it is sufficient to employ an affine clock error model given that Allan deviation can be neglected for a sufficiently small time period. Let t_i be the local time at target i, $i = \{1, 2\}$. The relation between the local time and the true time t is then modeled as an affine function,

$$t_i = \kappa_i t + \epsilon_i \Leftrightarrow \mathcal{C}_i(t_i) \triangleq t = \alpha_i t_i + \beta_i \tag{5.1}$$

where $\kappa_i \in \mathbb{R}_+$ and $\epsilon_i \in \mathbb{R}$ are the clock skew and the clock offset, respectively. Clock skew is a quantity to describe how fast the local clock drifts. It has no unit and can be interpreted as "given one time unit in true time, how much time is actually ticked in the local time in the same time unit". Hence, an ideal clock has skew equal to 1. As mentioned previously, the clock skew of low-cost OCXO or TCXO ranges between $[1 - 10^{-6}, 1 + 10^{-6}]$. The clock offset is the error accumulated up to time t_i, which should be 0 for an ideal clock. The skew and offset both are inherently time-varying, but in a short observation period of our system, they are modeled as constant [38]. The right part of 5.1 shows the inverse relation, where $[\alpha_i, \beta_i] \triangleq [\kappa_i^{-1}, -\kappa_i^{-1}\epsilon_i]$. They are calibration parameters needed to synchronize the local clock at target i with the true time.

5.2 Polynomial Relative Range Model

For a static pair of nodes, the relative range between them can be directly estimated since it is constant. For a pair of mobile nodes, however, the relative range is a function of time. In other words, at each time index the relative range is unique. It is then natural to approximate this nonlinear function by a polynomial function during a small observation period. Let $\tau_{ij} = c^{-1}d_{ij}$ be the propagation delay between the target i and j at some time instant, where d_{ij} is the relative range between i and j and c the speed of light. The propagation delay $\tau_{ij}(t)$ can be written as

$$\begin{aligned}\tau_{ij}(t) &= c^{-1}\mathcal{R}_{ij}(t) \\ &= c^{-1}(r_{ij}^{(0)} + r_{ij}^{(1)}t + r_{ij}^{(2)}t^2 + \cdots + r_{ij}^{(L-1)}t^{L-1})\end{aligned} \tag{5.2}$$

where $\mathcal{R}_{ij}(t)$ is used to model the time-varying pairwise range between target i and j and $\mathbf{r}_{ij} = [r_{ij}^{(0)}, r_{ij}^{(1)}, ...r_{ij}^{(L-1)}]^T \in \mathbb{R}^{L\times 1}$ contains all the coefficients of the approximation, which is not time-varying. L is the order of approximation and should be chosen according to the type of motion of targets.

Practically, the propagation delay $\tau_{ij}(t)$ is measured by targets with respect to their local clocks. So we substitute 5.1 into 5.2, we have the propagation delay as a function of local time t_i at target i in the following

$$\begin{aligned}\tau_{ij}(t) &= c^{-1}\mathcal{R}_{ij}(\mathcal{C}_i(t_i)) \\ &= c^{-1}(\gamma_{ij}^{(0)} + \gamma_{ij}^{(1)}t_i + \gamma_{ij}^{(2)}t_i^2 + \cdots + \gamma_{ij}^{(L-1)}t_i^{L-1})\end{aligned} \tag{5.3}$$

where on the right side of the equation above

$$\mathcal{G}_{ij}(t_i) = c^{-1}\mathcal{R}_{ij}(\mathcal{C}_i(t_i)) \tag{5.4}$$

represents the pairwise propagation delay with respect to the local time at target i. The range coefficients $\boldsymbol{\gamma}_{ij} = [\gamma_{ij}^{(0)}, \gamma_{ij}^{(1)}, ..., \gamma_{ij}^{(L-1)}]^T \in \mathbb{R}^{L\times 1}$ incorporate the range approximation parameters and the clock discrepancy of target i as well.

5.3 Mobile Pairwise Least Squares

As mentioned in Section 4.1, a pair of targets are able to communicate with each other. They communicate back and forth and signal transmission and receipt are timestamped at both sides independently with respect to the local clocks. Let K be the number of observation periods. In the kth observation period the corresponding timestamp recorded at node i is $T_{ij,k}$ and at node j it is $T_{ji,k}$. A timestamp can indicate transmission or receipt and it is determined by the direction of communication. Let $E_{ij,k} = \pm 1$ indicate the direction of communication. For example, when $E_{ij,k} = +1$ the signal is transmitted by node i and received by node j. When $E_{ij,k} = -1$ it is vice versa.

Now we have defined the set of time indices $k = \{1, 2, 3, ..., K\}$, so the signal propagation delay can be written as $\tau_{ij,k} = c^{-1}d_{ij,k}$, where $d_{ij,k}$ denotes the unique relative range between target i and j at time instant k.

Ideally, if the target pair are perfectly synchronized and noise-free, the kth timestamps marked at target i and j have the following relation

$$T_{ji,k} = \begin{cases} T_{ij,k} + c^{-1}d_{ij,k} & \text{for} i \rightarrow j \\ T_{ij,k} - c^{-1}d_{ij,k} & \text{for} i \leftarrow j \end{cases} \tag{5.5}$$

Using the direction indicator $E_{ij,k}$, this can be combined into one equation given by

$$\begin{aligned} T_{ji,k} &= T_{ij,k} + c^{-1}E_{ij,k}d_{ij,k} \\ &= T_{ij,k} + c^{-1}E_{ij,k}\mathcal{R}_{ij}(T_{ij,k}) \end{aligned} \tag{5.6}$$

where the pairwise range $d_{ij,k}$ is replaced by the value of relative range function $\mathcal{R}_{ij}(t_i)$ at time instant $T_{ij,k}$. To further incorporate the clock discrepancy, we rewrite the equation as

$$T_{ij,k} - T_{ji,k} + E_{ij,k}\mathcal{G}_{ij}(T_{ij,k}) = 0 \tag{5.7}$$

where all the timestamps are recorded with respect to the local time. To make the equation still hold under the asynchronous condition, we need to convert all timestamps to a standard time frame, namely the true time. Therefore, the clock model in 5.1 is substituted into 5.7 as

$$\mathcal{C}_i(T_{ij,k}) - \mathcal{C}_j(T_{ji,k}) + E_{ij,k}\mathcal{G}_{ij}(T_{ij,k}) = 0 \tag{5.8}$$

In reality, timestamps will also be contaminated by noise. For simplicity, it is modeled as white Gaussian noise. Therefore, we can further incorporate noise terms and rewrite the equation 5.8 as

$$\mathcal{C}_i(T_{ij,k} + \eta_{i,k}) - \mathcal{C}_j(T_{ji,k} + \eta_{j,k}) + E_{ij,k}\mathcal{G}_{ij}(T_{ij,k} + \eta_{i,k}) = 0 \tag{5.9}$$

where $\eta_{i,k}$ and $\eta_{j,k}$ represents the noise. Substitute the specific form of the clock model and relative range model into the equation, we get the following equation

$$\alpha_i T_{ij,k} - \alpha_j T_{ji,k} + \beta_i - \beta_j + E_{ij,k}(\gamma_{ij}^{(0)} + \gamma_{ij}^{(1)} T_{ij,k} + \gamma_{ij}^{(2)} T_{ij,k}^2 + \cdots) = \eta_{ij,k} \tag{5.10}$$

where all noise-related terms are absorbed by $\eta_{ij,k}$. Timestamps $T_{ij,k}$ and $T_{ji,k}$ recorded at time instant k at respective targets are measurements and the communication direction $E_{ij,k}$ at time instant k is also known. So the unknowns of the equation can be split into three categories: 1) $[\alpha_i, \beta_i]$ is the calibration parameter vector of the clock at target i; 2) $[\alpha_j, \beta_j]$ is the calibration parameter vector of the clock at the other target j; 3) $[\gamma_{ij}^{(0)}, \gamma_{ij}^{(1)}, \gamma_{ij}^{(2)}, ..., \gamma_{ij}^{(L-1)}]$ are the range coefficients we need to approximate the relative range between the target pair. Note that these parameters, under reasonable assumptions, are not time-varying. Therefore, it is intuitive to use the least-squares approach to solve this problem. This is referred to as mobile pairwise least squares in [36]. For K observation periods, K sets of data are acquired and K equations can be stacked.

Thus, a complete joint clock and range parameter model for K communications between a pair of targets i and j can be constructed as follows by stacking 5.10

$$[\boldsymbol{A}_{ij,1}, \boldsymbol{A}_{ij,2}] \begin{bmatrix} \alpha_i \\ \beta_i \\ \alpha_j \\ \beta_j \\ \gamma_{ij}^{(0)} \\ \gamma_{ij}^{(1)} \\ \vdots \\ \gamma_{ij}^{(L-1)} \end{bmatrix} = \boldsymbol{\eta}_{ij} \tag{5.11}$$

where

$$\boldsymbol{A}_{ij,1} = [\boldsymbol{t}_{ij}, -\boldsymbol{t}_{ji}\mathbf{1}_K, -\mathbf{1}_K] \tag{5.12}$$

$$\boldsymbol{A}_{ij,2} = \boldsymbol{E}_{ij}\boldsymbol{V}_{ij} \tag{5.13}$$

$$\boldsymbol{V}_{ij} = [\boldsymbol{t}_{ij}^{\odot 0}, \boldsymbol{t}_{ij}^{\odot 1}, ..., \boldsymbol{t}_{ij}^{\odot L-1}] \tag{5.14}$$

consist of the following vectors

$$\boldsymbol{t}_{ij} = [T_{ij,1}, ..., T_{ij,K}]^T \in \mathcal{R}^{K\times 1} \tag{5.15}$$

$$\boldsymbol{E}_{ij} = \text{diag}(\boldsymbol{e}_{ij}) \in \mathcal{R}^{K\times K} \tag{5.16}$$

$$\boldsymbol{e}_{ij} = [E_{ij,1}, ..., E_{ij,K}]^T \in \mathcal{R}^{K\times 1} \tag{5.17}$$

The time stamps recorded at target i and j during bidirectional communication are stored in $\boldsymbol{t}_{ij}$ and $\boldsymbol{t}_{ji}$, respectively. $\boldsymbol{e}_{ij}$ is a vector indicating the transmission direction for each data packet, which is also recorded at target i and j. Finally, the noise vector at the right side of the equation 5.11 is defined as

$$\boldsymbol{\eta}_{ij} = [\eta_{ij,1}, ..., \eta_{ij,K}]^T \in \mathcal{R}^{K\times 1} \tag{5.18}$$

According to [36], a time constraint is required in order to obtain a unique solution. In our case, it is convenient to assume, say, the clock of target i to be the time reference. By setting $\alpha_i = 1$ and $\beta_i = 0$, equation 5.10 can be rewritten as

$$T_{ij,k} - \alpha_j T_{ji,k} - \beta_j + E_{ij,k}(\gamma_{ij}^{(0)} + \gamma_{ij}^{(1)} T_{ij,k} + \gamma_{ij}^{(2)} T_{ij,k}^2 + \cdots) = \eta_{ij,k} \tag{5.19}$$

Stacking all data from K communications, we have the normal equation given by

$$\boldsymbol{A}_{ij}\boldsymbol{\psi}_{ij} = \boldsymbol{b}_{ij} + \boldsymbol{\eta}_{ij} \tag{5.20}$$

where

$$\boldsymbol{A}_{ij} = [-\boldsymbol{t}_{ji}, -\boldsymbol{1}_K, \boldsymbol{A}_{ij,2}] \in \mathcal{R}^{K\times(L+2)} \tag{5.21}$$

$$\boldsymbol{\psi}_{ij} = [\alpha_j, \beta_j, \boldsymbol{\gamma}_{ij}^T]^T \in \mathcal{R}^{(L+2)\times 1} \tag{5.22}$$

$$\boldsymbol{b}_{ij} = -\boldsymbol{t}_{ij} \tag{5.23}$$

For this problem, the least squares solution is then computed by

$$\hat{\boldsymbol{\psi}}_{ij} = \arg\min_{\boldsymbol{\psi}_{ij}} \|\boldsymbol{A}_{ij}\boldsymbol{\psi}_{ij} - \boldsymbol{b}_{ij}\|_2^2 = (\boldsymbol{A}_{ij}^T\boldsymbol{A}_{ij})^{-1}\boldsymbol{A}_{ij}^T\boldsymbol{b}_{ij} \tag{5.24}$$

5.4 Direction Estimation

Direction estimation refers to estimation of a three-dimensional unit vector that describes the azimuth and elevation information of target j with respect to target i. This direction vector is used by target i to solve the SoOp measurement equations in Chapter 3. We assume that all the UAVs are equipped with some device to estimate the direction of arrival (DOA) for signals coming from other UAVs. Again, this direction vector is time-varying.

Combining the estimated relative range $\mathcal{R}_{ij}(\mathcal{C}_i(t_i)) \in \mathcal{R}$ and the unit direction vector denoted by $\boldsymbol{\xi}_{ij}(t_i) \in \mathcal{R}^3$, the relative position $\Delta\boldsymbol{x}_i^{(p)} \in \mathcal{R}^3$, as a function of local time t_i at target i, can be written as

$$\Delta\boldsymbol{x}_i^{(p)} = \mathcal{R}_{ij}(\mathcal{C}_i(t_i))\boldsymbol{\xi}_{ij}(t_i) \tag{5.25}$$

5.5 Simulations

5.5.1 Results of joint ranging and synchronization

In this subsection, results of joint ranging and synchronization are presented. We use the identical set of UAV trajectories as that in Chapter4. The UAV network configuration is shown in Fig.4.5a. The mobile pairwise least squares (MGLS) is applied on every valid communication link in this network. It has been shown in [36] that the algorithm converge as long as the network is topologically a connected graph. To adhere to the needs of online processing, a moving window technique is also applied. The length of the rectangular window is $K = 500$. It is also the number of total communication, linearly distributed within a small period of 5 seconds. The ratio of forward and backward communication is $1 : 1$.

To evaluate the performance of the algorithm, the Root Mean Square Error (RMSE) metric is used. The RMSE errors are computed for the clock skew, the clock offset and the pairwise relative range. It is given by

$$\mathrm{RMSE}(\hat{\boldsymbol{\upsilon}}, \boldsymbol{\upsilon}) = \sqrt{N_{exp}^{-1} \sum_{n=1}^{N_{exp}} \|\hat{\boldsymbol{\upsilon}} - \boldsymbol{\upsilon}\|^2}, \tag{5.26}$$

where $\hat{\boldsymbol{\upsilon}}(n) \in \mathcal{R}^3$ is the n-th estimate and $\boldsymbol{\upsilon} \in \mathcal{R}^3$ is the unknown vector to be estimated.

On each communication link Monte Carlo experiments with the number of runs $N_{exp} = 50$ are performed. The order of relative range approximation is set to be $L = 3$. The initial clock skews and offsets of the deployed UAVs as well as that of the ground station are generated considering the typical values of low-cost oscillators mentioned in Section5.1. The skews of each UAV are generated randomly within the interval $[1 - 5\mathrm{ppm}, 1 + 5\mathrm{ppm}]$ while clock offsets are also generated randomly within the interval $[-5, 5]$ seconds. All the initial skews and offsets used in this experiment are shown in Table5.1. Without the loss of generality, the clock of the ground reference is set to have a skew of 1 and an offset of 0 second(s). The leader UAV is synchronized to the ground reference. Each follower UAV is synchronized to its neighbour which is "closer" to the leader UAV than itself (in the sense of the number of hops in the network to the leader).

The simulation results are shown in Table5.2. The RMSE of the clock skew estimation is at the magnitude of 10^{-10} and RMSE of the offset estimation is at the magnitude of 10^{-8}. RMSE of the pairwise range estimation is around 0.5 meters, regardless of different trajectories. Although the network shown in Fig.4.5a is not a full-mesh network, the algorithm still converges. Please note that the number of unique links in this experiment is equal to the minimum required number of links in order to preserve network connectivity. Another advantage of the mobile pairwise least squares (MPLS) is that it naturally works in a distributed fashion and can be easily adapted for online estimation.

Table 5.1: Initial skews and offsets of each UAV and the ground station

UAV ID	Clock skew	Clock offset(s)
0(ref)	1	0
1	$1-3\times10^{-6}$	3
2	$1-4\times10^{-6}$	4
3	$1+4\times10^{-6}$	4
4	$1+2\times10^{-6}$	-1
5	$1+3\times10^{-6}$	-2

Table 5.2: Tracking Performance of clock parameters and relative ranges

Link	RMSE skew	RMSE offset(s)	RMSE range(m)
$0 \longleftrightarrow 1$	3.1363×10^{-10}	1.8699×10^{-8}	0.4267
$1 \longleftrightarrow 2$	5.0049×10^{-10}	7.4569×10^{-8}	0.5419
$2 \longleftrightarrow 3$	3.6495×10^{-10}	4.2004×10^{-8}	0.4338
$2 \longleftrightarrow 4$	4.8012×10^{-10}	2.0695×10^{-8}	0.4854
$4 \longleftrightarrow 5$	4.8016×10^{-10}	1.9388×10^{-8}	0.3475

5.5.2 Results of cooperative localization with residual errors injected

Residual errors after synchronization will be translated into SoOp-based TDOA measurements as well as two-way ranging (TWR) relative range measurements. In this subsection, we present the simulation results with these residual errors injected.

Let us be more specific about the errors caused by local clocks. First, we look at leader UAVs that exploit ADS-B SoOp measurements. Recall the list of assumptions presented in Chapter 4, the whole network is considered static during an observation period sufficiently small; the clock skew and offset can thus be assumed constant within this observation period. Furthermore, we assume that the beacons, namely piloted aircraft providing ADS-B signals, are equipped with high-end clocks or oscillators that have a small skew. Under these assumptions, before synchronization is performed, the SoOp-based TDOA measurement model under asynchronous beacons and targets from [37] can be applied, which is given by

$$\rho_b = \left\|\boldsymbol{x}_t^{(p)} - \boldsymbol{x}_b^{(p)}\right\| - \left\|\boldsymbol{x}_r^{(p)} - \boldsymbol{x}_b^{(p)}\right\| + c\kappa_{t,r}\Delta T + c\epsilon_{t,r} + w_\rho \tag{5.27}$$

where $\boldsymbol{x}_t^{(p)}$, $\boldsymbol{x}_r^{(p)}$, $\boldsymbol{x}_b^{(p)} \in \mathcal{R}^3$ are positions of the target t, the reference r, and the beacon b; $\kappa_{t,r} = 1/\kappa_r - 1/\kappa_t$ is the relative clock skew between the target t and its reference r; $\epsilon_{t,r}$ is the relative bias accumulated up to now. c is the speed of light.

If we manage to do synchronization between the reference and the target (leader) by estimating the clock skew and offset of the target, denoted by $\hat{\kappa_t}$ and $\hat{\epsilon}_{t,r}$, the corrected TDOA measurement is then given by

$$\hat{\rho_b} = \left\|\boldsymbol{x}_t^{(p)} - \boldsymbol{x}_b^{(p)}\right\| - \left\|\boldsymbol{x}_r^{(p)} - \boldsymbol{x}_b^{(p)}\right\| + c(\kappa_{t,r} - \hat{\kappa_{t,r}})\Delta T + c(\epsilon_{t,r} - \hat{\epsilon}_{t,r}) + w_\rho \tag{5.28}$$

where $\hat{\kappa_{t,r}} = 1/\kappa_r - 1/\hat{\kappa}_t$. The last three terms in the equation above consist of the residual errors after synchronization. Here the local clock of the reference is considered as the standard clock, hence $\kappa_r = 1$. In simulations, we store the estimated clock skews and offsets and compute the error terms $c(\kappa_{t,r} - \hat{\kappa_{t,r}})\Delta T$ and $c(\epsilon_{t,r} - \hat{\epsilon}_{t,r})$. Then we inject the errors into generated SoOp-based TDOA measurements.

For follower UAVs, relative ranges are obtained simultaneously with clock calibration parameters, as mentioned in Section5.3. The ranging accuracy of mobile pairwise least squares (MPLS) is shown in the section above. Hence, we inject the relative range errors by augmenting the standard deviation of TWR sensor measurement noise, which is among simulation parameters listed in Table4.1.

Other key simulation parameters are identical to that in Table4.1. Monte Carlo experiments are conducted with residual errors injected. A snapshot of the estimated trajectory of UAV 1 in one simulation run is visualized in Fig.5.1, with corresponding error plots shown in Fig.5.2. Complete results of Monte Carlo experiments are shown in Table5.3, 5.4, and 5.5. It is observed that residual errors make the navigation performance degrade. Larger errors in TWR measurements also make the performance degradation caused by increasing D(h) values more severe, compared to that in Section4.4.3 and 4.4.6. Despite that, the proposed algorithm still converges and shows robustness against synchronization errors.

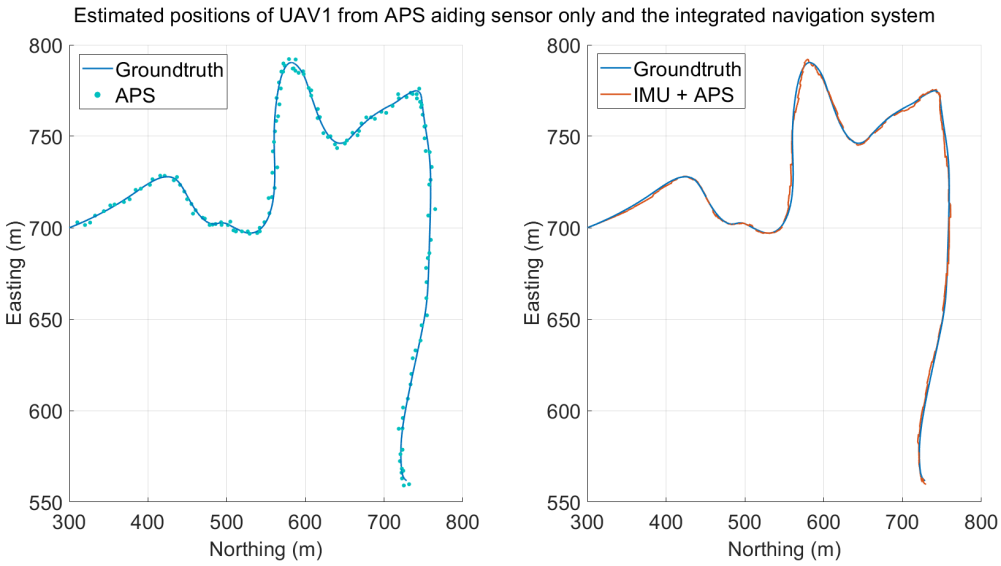

Figure 5.1: Simulation with residual errors injected: UAV 1 estimated trajectory

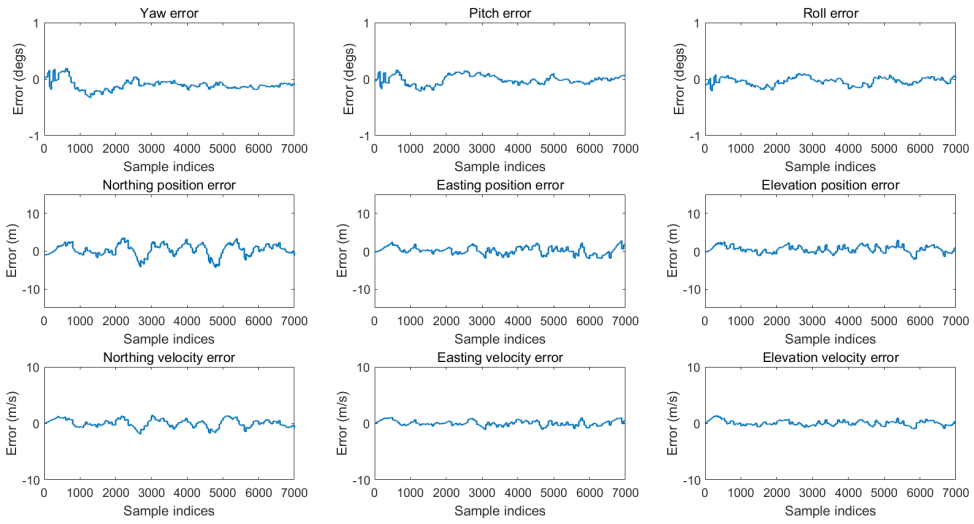

Figure 5.2: Simulation with residual errors injected: UAV 1 tracking errors

Table 5.3: Simulation with residual errors injected: orientation tracking performance (APS + IMU)

UAV ID	AMSE($degs^2$)	RMSE(degs)	MAE(degs)
1	0.0572	0.2391	0.2065
2	0.0579	0.2407	0.2076
3	0.1754	0.4188	0.3778
4	0.2285	0.4780	0.4208
5	0.0665	0.2578	0.2243

Table 5.4: Simulation with residual errors injected: position tracking performance (APS + IMU)

UAV ID	AMSE(m^2)	RMSE(m)	MAE(m)
1	13.19	2.90	2.29
2	14.09	3.11	2.47
3	14.79	3.28	2.60
4	14.70	3.26	2.59
5	15.72	3.46	2.74

Table 5.5: Simulation with residual errors injected: velocity tracking performance (APS + IMU)

UAV ID	AMSE(m^2/s^2)	RMSE(m/s)	MAE(m/s)
1	2.38	1.25	1.00
2	2.55	1.34	1.07
3	2.67	1.40	1.12
4	2.67	1.40	1.12
5	2.83	1.48	1.19

6 Conclusion and Future Work

6.1 Conclusion

In this thesis, we propose a novel framework of cooperative localization in order to provide a group of small unmanned aerial vehicles (UAVs) with alternative positioning, navigation, and timing (APNT) service in GNSS-denied environments. The proposed algorithms are simulated in the scene of multi-UAV cooperative localization and the effectiveness of the algorithms are verified. The main contributions of this thesis are as follows.

- We propose that ADS-B signals from piloted aircraft can be exploited as signal of opportunity for navigation purposes. We analyze what information and physical properties can be extracted from ADS-B signals. Based on the analysis, an SoOp-based TDOA configuration is chosen for this problem. By leveraging ADS-B SoOp, UAVs do not require dedicated APNT infrastructure to provide navigation signals, though a ground reference station is still needed.
- We propose a leader-follower strategy for cooperative localization of multiple UAVs based on inter-UAV communication networks. By leveraging this strategy, the service burden of the ground reference station is reduced. It is further verified on synchronized UAV networks with different topological configurations. Additionally, an empirical observation from Monte Carlo experiments is that the proposed algorithm does not need a full-mesh inter-UAV network to converge.
- An EKF-based sensor fusion algorithm is designed for individual UAV navigation. It fuses data from a low-cost IMU and an aiding sensor (ADS-B SoOp sensor or TWR sensor). The proposed algorithm is verified in a multi-UAV scene with practical simulation parameters, showing its robustness against varying number of available beacons, varying beacon uncertainty, and variation of network topology. The proposed algorithm achieves an overall performance comparable to civilian GNSS in our experiments. Meanwhile, we acknowledge that many other factors can have an influence, e.g. geometric distribution of beacons, radio wave propagation, hardware implementation, which are not considered and out of the scope of this thesis. Hence, this conclusion is restricted in selected data sets and simulation settings.
- We identified how errors caused by asynchronous clocks can be translated into both absolute and relative position measurements. A joint relative positioning and synchronization algorithm is applied to tackle this problem. The pairwise version of this algorithm is verified in a scene of five UAVs. Furthermore, this algorithm does not increase the minimum connectivity requirement of inter-UAV networks.

With this algorithm, the cooperative localization strategy can be further extended to a network of asynchronous UAVs.

6.2 Future Work

The work of this thesis can be further improved from the following aspects.

First, for ADS-B SoOp, there are more specific problems remain unaddressed. The success of ADS-B SoOp relies on a good estimation of signal time of arrival (TOA). It is then a problem of how precise TOA estimation needs to be. Based on the precision requirement, some TOA estimation techniques such as [29] can be used.

Second, in [36] it is shown that mobile global least squares (MGLS) outperforms mobile pairwise least squares(MPLS) in certain networks. Therefore, MGLS can be applied to further reduce synchronization errors. For a network of UAVs, distributed processing is often favoured. Hence, a distributed version of MGLS suitable for UAV applications may be of interest.

Bibliography

[1] S. Han, Z. Gong, W. Meng, C. Li, and X. Gu, "Future alternative positioning, navigation, and timing techniques: A survey," *IEEE Wireless Communications*, vol. 23, pp. 154–160, 2016.

[2] D. Constantine, "The future of the drone economy," 2020, [Online].

[3] Research and Markets, "Drone service market - global forecast to 2025," 2019, [Online].

[4] R. Morales-Ferre, P. Richter, E. Falletti, A. de la Fuente, and E. S. Lohan, "A survey on coping with intentional interference in satellite navigation for manned and unmanned aircraft," *IEEE Communications Surveys & Tutorials*, vol. 22, pp. 249–291, 2020.

[5] S. C. Lo, B. B. Peterson, D. M. Akos, M. J. Narins, R. Loh, and P. K. Enge, "Alternative position navigation & timing (apnt) based on existing dme and uat ground signals," 2011.

[6] S. L. Jheng, S.-S. Jan, Y. Chen, and S. C. Lo, "1090 mhz ads-b-based wide area multilateration system for alternative positioning navigation and timing," *IEEE Sensors Journal*, vol. 20, pp. 9490–9501, 2020.

[7] W. Tang, J. Chen, C. Yu, J. Ding, and R. Wang, "A new ground-based pseudolite system deployment algorithm based on mopso," *Sensors (Basel, Switzerland)*, vol. 21, 2021.

[8] H. Liu, L. Zhao, X. Huang, and Q. Tang, "A technique of time synchronization in pseudolite system based on single-difference method," *Journal of Physics: Conference Series*, vol. 1732, 2021.

[9] S. Ramasamy, A. Gardi, and R. Sabatini, "Uav navigation using signals of opportunity in urban environments: An overview of existing methods," 2017.

[10] N. Ruseno, C.-Y. Lin, and S.-C. Chang, "Uas traffic management communications: The legacy of ads-b, new establishment of remote id, or leverage of ads-b-like systems?" *Drones*, 2022.

[11] S. Deshpande, "Terrapoint - an advanced terrestrial technology to enhance navigation in a gnss-denied environments," *Proceedings of the 34th International Technical Meeting of the Satellite Division of The Institute of Navigation (ION GNSS+ 2021)*, 2021.

[12] J. Khalife, S. Bhattacharya, and Z. M. Kassas, "Centimeter-accurate uav navigation with cellular signals," *Proceedings of the 31st International Technical Meeting of The Satellite Division of the Institute of Navigation (ION GNSS+ 2018)*, 2018.

[13] J. Khalife and Z. Kassas, "Opportunistic uav navigation with carrier phase measurements from asynchronous cellular signals," *IEEE Transactions on Aerospace and Electronic Systems*, vol. 56, pp. 3285–3301, 2020.

[14] Y. Zeng, X. Xu, S. Jin, and R. Zhang, "Simultaneous navigation and radio mapping for cellular-connected uav with deep reinforcement learning," *IEEE Transactions on Wireless Communications*, vol. 20, no. 7, pp. 4205–4220, 2021.

[15] J. J. Morales, J. J. Khalife, and Z. M. Kassas, "Information fusion strategies for collaborative inertial radio slam," *IEEE Transactions on Intelligent Transportation Systems*, pp. 1–18, 2021.

[16] T. Qin, P. Li, and S. Shen, "Vins-mono: A robust and versatile monocular visual-inertial state estimator," *IEEE Transactions on Robotics*, vol. 34, pp. 1004–1020, 2018.

[17] Z. Gong, P. Liu, F. Wen, R. Ying, X. Ji, R. Miao, and W. Xue, "Graph-based adaptive fusion of gnss and vio under intermittent gnss-degraded environment," *IEEE Transactions on Instrumentation and Measurement*, vol. 70, pp. 1–16, 2021.

[18] EUROCONTROL, "Regulation (eu) 2020/587 by european union aviation safety agency," retrieved from https://eur-lex.europa.eu/legal-content/EN/TXT/?uri=CELEX:32020R0587.

[19] t. U. S. Federal Aviation Administration, "Code of federal regulations by federal aviation administration," retrieved from https://www.ecfr.gov/current/title-14/chapter-I/subchapter-F/part-91/subpart-C/section-91.225.

[20] J. Sun, "The 1090 megahertz riddle: A guide to decoding mode s and ads-b signals," 2021.

[21] B. W. Parkinson and J. J. Spilker, "Global positioning system : theory and applications," 1996.

[22] P. K. Enge, "The global positioning system: Signals, measurements, and performance," *International Journal of Wireless Information Networks*, vol. 1, pp. 83–105, 1994.

[23] G. Welch and G. Bishop, "Welch & bishop , an introduction to the kalman filter 2 1 the discrete kalman filter in 1960," 1994.

[24] K. Fisher, "The navigation potential of signals of opportunity-based time difference of arrival measurements," 2005.

[25] M. Guterres, S. R. Jones, G. L. Orrell, and R. Strain, "Ads-b surveillance system performance with small uas at low altitudes," 2017.

[26] C. W. Lum, H. Rotta, R. Patel, H. Kuni, T. Patana-anake, J. Longhurst, and K. Chen, "Uas operation and navigation in gps-denied environments using multilateration of aviation transponders," *AIAA Scitech 2019 Forum*, 2019.

[27] T. L. Verbraak, J. Ellerbroek, J. Sun, and J. M. Hoekstra, "Large-scale ads-b data and signal quality analysis," 2017.

[28] J. F. Raquet, M. M. Miller, and T. Nguyen, "Issues and approaches for navigation using signals of opportunity," 2007.

[29] R. Calvo-Palomino, F. Ricciato, B. Repas, D. Giustiniano, and V. Lenders, "Nanosecond-precision time-of-arrival estimation for aircraft signals with low-cost sdr receivers," *2018 17th ACM/IEEE International Conference on Information Processing in Sensor Networks (IPSN)*, pp. 272–277, 2018.

[30] X. R. Li and V. P. Jilkov, "Survey of maneuvering target tracking. part i. dynamic models," *IEEE Transactions on Aerospace and Electronic Systems*, vol. 39, pp. 1333–1364, 2003.

[31] ——, "Survey of maneuvering target tracking. part v. multiple-model methods," *IEEE Transactions on Aerospace and Electronic Systems*, vol. 41, pp. 1255–1321, 2005.

[32] M. Kok, J. D. Hol, and T. B. Schön, "Using inertial sensors for position and orientation estimation," *ArXiv*, vol. abs/1704.06053, 2017.

[33] J. F. A. Alarcón, F. J. S. Nieto, and J. G.-H. Carretero, "Aircraft used as a sensor for atmospheric behaviour determination. practical case: pressure estimation using automatic dependent surveillance-broadcast," *Proceedings of the Institution of Mechanical Engineers, Part G: Journal of Aerospace Engineering*, vol. 227, pp. 778 – 797, 2013.

[34] M. Fonder and M. V. Droogenbroeck, "Mid-air: A multi-modal dataset for extremely low altitude drone flights," in *Conference on Computer Vision and Pattern Recognition Workshop (CVPRW)*, June 2019.

[35] L. Pan and F. Guo, "Real-time tropospheric delay retrieval with gps, glonass, galileo and bds data," *Scientific Reports*, vol. 8, 2018.

[36] R. T. Rajan and A.-J. van der Veen, "Joint ranging and synchronization for an anchorless network of mobile nodes," *IEEE Transactions on Signal Processing*, vol. 63, pp. 1925–1940, 2015.

[37] M. Leng, F. Quitin, W. P. Tay, C. Cheng, S. G. Razul, and C. M. S. See, "Anchor-aided joint localization and synchronization using soop: Theory and experiments," *IEEE Transactions on Wireless Communications*, vol. 15, pp. 7670–7685, 2016.

[38] N. M. Freris, S. R. Graham, and P. R. Kumar, "Fundamental limits on synchronizing clocks over networks," *IEEE Transactions on Automatic Control*, vol. 56, pp. 1352–1364, 2011.